Systematic spatio-temporal mapping reveals divergent cell death pathways in three mouse models of hereditary retinal degeneration

Power M.J.[1-3], Rogerson L.E.[1-5], Schubert T.[1,2], Berens P.[1, 2,4,5], Euler T.[1,2,4#], Paquet-Durand F.[1#]

[1] Institute for Ophthalmic Research, University of Tübingen, Elfriede-Aulhorn-Strasse 7, 72076 Tübingen, Germany

[2] Centre for Integrative Neuroscience (CIN), University of Tübingen, Otfried-Müller-Str. 25, 72076 Tübingen, Germany

[3] Graduate Training Centre of Neuroscience (GTC), University of Tübingen, Österbergstraße 3, 72074 Tübingen, Germany

[4] Bernstein Center for Computational Neuroscience, Otfried-Müller-Str. 25, 72076 Tübingen, Germany

[5] Department of Computer Science, University of Tübingen, Sand 14, 72076 Tübingen, Germany

[#] Co-corresponding authors

Keywords: retina, cGMP, CNG channel, calpain, calcium, Gaussian process modelling

Abstract

Calcium (Ca^{2+}) dysregulation has been linked to neuronal cell death, including in hereditary retinal degeneration. Ca^{2+} dysregulation is thought to cause rod and cone photoreceptor cell death. Validation of this hypothesis has been hampered so far by spatial and temporal heterogeneities in retinal disease models.

Here, we examined the role of Ca^{2+} in photoreceptor degeneration by assessing the activation pattern of Ca^{2+}-dependent calpain proteases. We generated spatio-temporal maps of the entire retina in the *cpfl1* mouse model for primary cone degeneration, as well as for primary rod degeneration in *rd1* and *rd10* mutant mice. In the latter two models, the spatio-temporal pattern of increased calpain activity matched the progression of primary rod degeneration. High calpain activity coincided with activation of the calpain-2 isoform but not with calpain-1, suggesting differential roles for the two calpain isoforms. Furthermore, primary rod loss was associated with an upregulation of apoptosis-inducing factor (AIF), even though only a minute fraction of cells showed activity of the apoptotic marker caspase-3. However, after the conclusion of primary rod degeneration, caspase-3 activation appeared in cones, suggesting apoptosis as the dominant mechanism for secondary cone loss. To distinguish the temporal sequences of degenerative molecular processes from other sources of variability, we used Gaussian process models, which highlighted calpain activity as a key event during primary rod photoreceptor cell death.

Taken together, our data suggests a causal link between Ca^{2+} dysregulation and primary, non-apoptotic degeneration of photoreceptors. On the other hand, it also suggests a role for apoptosis in secondary degeneration of cones. This systematic investigation of retinal

degeneration highlights the importance of the spatial and temporal location of key molecular events, and may guide the design of future studies, including the evaluation of new therapies.

Introduction

The primary light-detecting cells in the retina are rod and cone photoreceptors (rods and cones). Generally, cones are responsible for day time vision, while rods are responsible for vision under dim light conditions. Rods and/or cones degenerate and die in a heterogeneous group of genetic diseases called hereditary retinal degeneration (RD). The most common disease within this group is Retinitis Pigmentosa (RP), which first causes the loss of rods, followed by secondary cone loss. Approximately one in 3,500 individuals is affected by RP (Bertelsen et al., 2014), which presents in humans as a progressive loss of night vision, gradual constriction of the visual field ("tunnel vision"), and eventually complete blindness (Hartong et al., 2006). A related retinal dystrophy is achromatopsia, affecting about one in 30,000 individuals (Remmer et al., 2015), in which typically only the cones are lost.

Autosomal recessive forms of RP in humans are caused, for instance, by mutations in the rod-specific phosphodiesterase 6B (*PDE6B*) (Danciger et al., 1995; Hamel, 2006; McLaughlin et al., 1993). Conversely, mutations in the cone-specific *PDE6C* are a hallmark of achromatopsia (7). The function of PDE6 is to hydrolyse cyclic guanosine monophosphate (cGMP) after light detection, initiating the photoreceptor signalling cascade. Loss of PDE6 activity in either rods or cones results in higher-than-normal levels of intracellular cGMP, leading to constitutive opening of cyclic-nucleotide-gated (CNG) channels (8,9). This in turn leads to a cation influx carried mostly by Na^+ and Ca^{2+} (Arango-Gonzalez et al., 2014; Michalakis et al., 2018)

Strict regulation of the intracellular Ca^{2+} concentration ($[Ca^{2+}]$) is essential for the function and survival of neurons and therefore tightly controlled by several mechanisms across cellular compartments (as reviewed in Krizaj & Copenhagen, 2002). Dysregulation of $[Ca^{2+}]$ has been theorized to initiate photoreceptor cell death, but the underlying mechanisms are still debated. For instance, high $[Ca^{2+}]$ has been proposed to trigger apoptosis (Orrenius et al., 2003),

however, apoptotic caspases do not appear to be activated in most animal models for RD (Arango-Gonzalez et al., 2014; Doonan et al., 2005). Of note in this context is the mitochondrial membrane protein apoptosis-inducing factor (AIF). Despite its name, AIF is associated with non-apoptotic, necrosis-like forms of cell death (15), as its function does not require caspase activity (16) and has previously been linked to cell death in photoreceptors (Sanges et al., 2006).

Strong indication for Ca^{2+} involvement in photoreceptor cell death comes from the finding of stalwartly increased calpain activity as a common denominator in many RD models (10). Calpains comprise a family of Ca^{2+}-activated cysteine proteases with 15 isoforms identified to date (18). Some are ubiquitously expressed throughout the body (*e.g.* calpain-1, -2), others are tissue-specific (*e.g.* calpain-3, -8) (Suzuki et al., 2004). While calpain-1 is considered to be neuroprotective, calpain-2 may be involved in neurodegeneration (20). The two isoform's Ca^{2+} affinities may indicate their presumed functions: calpain-1 activates at around 5 to 50 µM, which is much less than the ~1 mM needed for calpain-2 activation (21). Hence, excessive calpain-2 activation as a consequence of [Ca^{2+}] dysregulation has long been linked to cell death mechanisms, but its exact role is still controversial (reviewed in Liu, Van Vleet, & Schnellmann, 2004; Rizzuto et al., 2003; Baudry & Bi, 2016).

To elucidate the degenerative progression, we performed spatio-temporal mapping in the RD and wt retina to assess the levels of calpain activity, as well as the expression of several other enzymes related to cell death, including calpain-1, calpain-2, AIF and caspase-3. To study primary cell death of both cone and rod photoreceptors, we employed the cone-photoreceptor-function loss (*cpfl1*) mouse model for achromatopsia (Chang et al., 2009) and the retinal degeneration mouse models *rd1* (Keeler, 1966) and *rd10* (Chang et al., 2002), both considered to be models for RP. In *rd1* and *rd10*, in addition to primary rod loss, we also studied secondary degeneration of cones. We applied probabilistic modelling to predict a likely

sequence of degenerative events in the different mutant models. Our data suggests that during the initial stages of degeneration in RP, calpain-2 is strongly activated, while calpain-1 activation appears later. This points at the execution of non-apoptotic cell death mechanisms during primary rod degeneration. However, a delayed activation of caspase-3 in *rd1* cones suggests that secondary cone degeneration is instead caused by "classical" caspase-driven apoptosis.

Material and Methods

Animals. To study primary cone and rod degeneration, *cpfl1* (C57BL/6J background) and *rd1* (C57BL/6J x C3H background) mutant mice were used. We additionally used the more slowly degenerating *rd10* mice (C57Bl6/J) to assess primary rod degeneration at a longer timescale than in *rd1*, because in *rd10* retina, developmental and degenerative cell death are temporally less overlapping (10,27). Animals from all lines were used irrespective of gender. Wild-type and mutant *rd1* and *cpfl1* mice were crossbred with the transgenic mouse line *HR2.1:TN-XL* (C57BL/6J background), which expresses the Ca^{2+} biosensor TN-XL (28) under the control of the human red opsin promoter (HR2.1) selectively in cone photoreceptors (29). The mouse lines thereby generated were the *HR2.1:TN-XL* x *cpfl1* and *HR2.1:TN-XL* x *rd1* lines; for simplicity, we refer to these biosensor lines in the following as wt, *cpfl1*, and *rd1*. In the context of the present study, these mouse lines allowed for a direct identification of cones. Animals older than postnatal day 12 (P12) were sacrificed by CO_2 asphyxiation followed by cervical dislocation. Mice younger than P12 were sacrificed by decapitation. All procedures were performed in accordance with the law on animal protection issued by the German Federal Government (Tierschutzgesetz) and approved by the institutional animal welfare office of the University of Tübingen.

Calpain activity assay. Following earlier work (Kulkarni et al., 2016), calpain activity was initially analysed in mice at P14, 18, 24, 30, 60, 90 and 120 (Supplemental Table 1). In early degeneration *rd1* mouse and, for comparison, in wt animals, we added P10 and P12. Eyes were marked on the nasal side prior to enucleation, flash-frozen in liquid nitrogen, embedded in Tissue-Tek OCT compound (Sakura Finetek Europe, Alphen aan Den Rijn, Netherlands), and stored at -20°C until cryo-sectioning into 16 µm thick vertical sections. Sections were rehydrated in calpain reaction buffer (CRB; in g: 5.96 HEPES, 4.85 KCl, 0.47 $MgCl_2$, 0.22 $CaCl_2$ in 100ml ddH_2O; pH 7.2) with 2 mM dithiothreitol (DTT), and then incubated for 2 h at 37°C in CRB containing 50 µM of tBOC-Leu-Met-CMAC (Molecular Probes), a calpain-specific substrate, whose fluorescence increases after cleavage by calpain (Paquet-Durand et al., 2006).

Immunohistochemistry. We analysed mice at P10, 12, 14, 18, 24, and 30 (Supplemental Table 1). Due to the lack of a discernible outer nuclear layer (ONL) in *rd1* and *rd10* animals after P30, and the lack of significant difference in calpain activity in *cpfl1* and wt post P30-animals, we limited our examination to time-points between P10 and P30. Eyes were fixed in 4% PFA in 0.1 M phosphate buffer saline (PBS, pH 7.4; for 45 min) and cryo-protected in sucrose gradients in PBS at room temperature for 2 hrs. Then, eyes were embedded in Tissue-Tek OCT compound (Sakura Finetek Europe, Alphen aan Den Rijn, Netherlands) and stored at -20°C until cryo-sectioning into 16 µm thick vertical sections. Sections were rehydrated with PBS, permeabilized in 0.3% Tween in PBS containing blocking solution (10% goat serum, 1% BSA). As primary antibodies, we used rabbit anti-calpain-2 (ab39165; 1:300; Abcam, Cambridge, UK), rabbit anti-calpain-1 (ab39170; 1:100; Abcam, Cambridge, UK), rabbit anti-cleaved-caspase-3 (#9664; 1:300, Cell Signalling Technology, Frankfurt, Germany), and

rabbit anti-AIF (ab1998; 1:350; Abcam, Cambridge, UK). As secondary antibodies, we used goat anti-rabbit Alexa Fluor 488 (1:350; Molecular Probes, Eugene, USA).

Cell death detection: Mice were analysed at P10, 12, 14, 18, 24, and 30 (Supplemental Table 1). The terminal deoxynucleotidyl transferase dUTP nick end labelling (TUNEL) assay was performed using the TMR red kit from Roche Diagnostics (Mannheim, Germany). Sections were incubated in blocking solution (1% BSA, 10% normal goat serum, 1% fish gelatine) for 1 hr after 5 min incubation with alcohol acetic acid mixture (62% EtOH, 11% Acetic Acid, 27% H_2O). Sections were then stained using TMR red TUNEL kit as per manufacturer's instructions.

Microscopy and image processing. Z-stack images were captured on an Imager Z1 ApoTome microscope using a 20x air objective (0.8 NA; *cf.*), and Zen (v.2.3 Pro) software (Carl Zeiss Microscopy GmbH, Oberkochen, Germany). Zen Lite v.2.3 software was used to reconstruct images and ImageJ 1.52e (http://imagej.nih.gov/ij) was used to count positive markers in each image. Figures were generated in IGOR Pro (Wavemetrics, Lake Oswego, USA) and arranged in Canvas 11 (ACD Systems International Inc., Seattle, USA).

Analysis of marker data. Data was obtained from at least three different animals for each parameter examined. For each animal, vertical sections were quantified, using collapsed Z-stacks of n= 10-22 images, spaced at 0.75 µm z-distance, acquired at 20x magnification (Methods Fig. 1). For each section, five regions across the retina were imaged and analysed. Here, the central retina was taken as the medial portion along both the dorso-ventral and naso-temporal axis, as well as, dorsomedial and ventromedial sections close to the optic nerve. Calpain-active, as well as calpain-2-, calpain-1-, caspase-3-, AIF-, and TUNEL-labelled cells

were counted and expressed as number of positive cells in the ONL per 1,000 μm² in all mouse lines, and at all time-points. Statistical comparisons were made using the Kruskal–Wallis one-way analysis of variance test using GraphPad Prism 7 (La Jolla, USA). Statistical comparisons were confined to different mouse lines of the same age and not across ages.

Gaussian process modelling. Gaussian Process models (GPs) (32) were used to estimate the mean and standard deviation of the activity of each cell death marker, for each mouse line, at the observed time-points. These models were used as they are able to accommodate the non-linear change in the level of each marker, and provide a generative model for estimating properties of interest (in our case, the likely peaks for each marker). Modelling was performed in Python 3.5 using the GPy (33) library.

Prior to model fitting, a square root transformation was applied to the observed activity of each marker to accommodate the left-skew and zero-bound; the inverse transformation was applied for subsequent inference. The GPs inferred how the observed activity of each marker, *y*, varied over time, *x*, for each mouse line. The GP (Eq. 1) was defined by the mean activity function $\mu(x)$, the covariance of this activity $K(x, x')$ (Eq. 2), and additive zero-mean Gaussian observation noise ε (Eq. 3). A radial basis function kernel was used to model the covariance of the signal over time. The model was parameterised by the signal variance σ^2_{noise}, length scale l, and noise variance σ^2_{noise}; these parameters were inferred using the L-BFGS-B maximum likelihood algorithm.

$$\sqrt{y} = GP\left(\mu(x), K(x, x');\ \sigma^2_{signal}, l\right) + \varepsilon$$

$$K(x, x') = \sigma^2_{signal} \exp\left(-\frac{(x - x')^2}{2l^2}\right)$$

$$\varepsilon = N(0, \sigma^2_{noise})$$

Once fitted, the GPs could be used as generative models to compute bootstrap estimates of molecular sequences. We drew 10,000 samples from each model and identified the maxima in each sample. The marginal distribution of these maxima was used as an estimate of the timing of the peak of activity in each model. For each of the samples, we also identified the relative ordering of the peaks of each molecular marker, to derive an approximate molecular sequence. The probability of any given molecular sequence was calculated as the number of times it was present in these samples, as a proportion of the total number of samples which were drawn from the models. We excluded those sequences that had a probability of 0.05 or lower.

Generation of heat maps. During retinal sectioning, order and orientation of sections were maintained (Methods Fig. 1). Hence, the retinal location of each image could be determined using the section number and the distance from the optic nerve head along the section, providing x- (nasal-temporal) and y-coordinates (dorsal-ventral), respectively. To visualise the spatio-temporal progression of the markers, the mean activity at each location along the dorsal-ventral axis was used (averaging over the nasal-temporal dimension) and plotted against each time-point. Heat-maps were generated in Python 3 using the matplotlib library.

Results

To link Ca^{2+} dysregulation to photoreceptor cell death, we utilised RD mouse models with mutations in *Pde6* genes. The *rd1* and *rd10* lines carry different mutations in the *Pde6b* gene, whereas the *cpfl1* line suffers from a mutation in the homologous, cone-specific *Pde6c* gene. To align our experiments with earlier studies of mouse photoreceptor degeneration, we first compared changes in outer nuclear layer (ONL) thickness over the first post-natal month

between the mutants and wt mice (Fig. 1). The number of photoreceptor rows dramatically decreased in post-P12 *rd1* and in *rd10* after P18, illustrating the difference in onset of photoreceptor cell death in these models (10). The *rd10* degeneration is less aggressive than *rd1* as it takes longer for complete ablation of the ONL in *rd10* than in *rd1*. In contrast, in the cone degeneration *cpfl1* mutant the ONL thickness remains similar to wt, because in mice, rods outnumber cones by a factor of 25 to 50 (Jeon, Strettoi, & Masland, 1998, Behrens et al., 2016), and primary cone loss does not produce secondary rod loss.

Calpain activity increases in ONL of degenerating retina

We next aimed at elucidating the role of Ca^{2+} dysregulation in photoreceptor cell death. To this end, we focussed first on the activity and regulation of Ca^{2+}-dependent calpain-type proteases, which can be considered as surrogate markers for Ca^{2} dysregulation (Croall & Ersfeld, 2007; Goll et al., 2003). In *rd1* retina, the number of ONL cells showing increased calpain activity was significantly higher compared to wt and *cpfl1*, at all time-points, with a peak of activity at P12 (Fig. 2A, D; for detailed statistics of all comparisons, see Supplemental Table 2). Calpain activity in *rd10* ONL was also significantly increased compared to wt and *cpfl1* (at P18, 24, and 30), peaking around P18 (Fig. 2B, D). In c*pfl1*, calpain activity tended to be higher than in wt, yet, without a clear peak within the inspected time frame (Fig. 2C, D). Overall, *rd1* retinae displayed the highest levels of calpain activity. These data are in line with other studies (Arango-Gonzalez et al., 2014; Paquet-Durand et al., 2006) that showed increases in calpain activity at specific time-points in models of RP and achromatopsia.

Activation of calpain-2, but not calpain-1, increases during disease progression

We then investigated whether the high levels of calpain activity observed in the ONL could be attributed to specific calpain isoforms. We focussed on calpain-1 and calpain-2, which have

been reported to be ubiquitously expressed in all mammalian cells and to play opposite roles in neurodegeneration (Chen et al., 2007; Goñi-Oliver et al., 2007). We hypothesized that calpain-2 may contribute to the observed increased calpain activity, as it requires a high [Ca^{2+}] that is considered beyond the physiological range of photoreceptors (Goll, 1995). Using antibodies recognizing the activated proteases, we found significantly increased numbers of calpain-2 positive cells in both *rd1* and *rd10* ONL, when compared to *cpfl1*, as well as to wt controls (Fig. 3A, B, D; for all statistics, see Supplemental Table 2). The peaks appeared to coincide with those for the calpain assay, namely at P12 (*rd1*) and P18 (*rd10*). In *cpfl1*, the number of calpain-2 positive cells was slightly increased over the wt level (Fig. 3C, D), however, without a clear peak. To our surprise, a significant increase in calpain-1 positive cell numbers from wt level was observed in *rd10* (Supplemental Fig. 1A-C). Calpain-1 labelling increased over background levels around P18 and was even more pronounced at the end of the observed time window (P30) (Supplemental Fig. 1D). Next to *rd10*, only *rd1* showed a detectable (but not significant) increase in calpain-1 positive cell counts.

Taken together, we found differential patterns of calpain isoform activation: While calpain-2 was strongly activated in *rd1* and *rd10* (and much less so in *cpfl1*), calpain-1 was more strongly activated in *rd10* compared to the other lines. Moreover, the calpain-2 expression peak coincides with the peak of calpain activity assay data and precedes that of calpain-1.

Cell death coincides with calpain activity

To compare the activity and expression of calpain in the ONL with the incidence of cell death, we used the TUNEL assay, which labels nick-ends in a cell's DNA. While TUNEL is an excellent marker for cell death, for the present study it is important to mention that TUNEL does not discriminate between different cell death mechanism(s) (41). In agreement with earlier work (10), we found significantly increased numbers of TUNEL-positive cells in *rd1* and *rd10* ONL (Fig. 4A, B, D: for all statistics, see Supplemental Table 2). A slight increase

in TUNEL-positive cell number was also seen in the *cpfl1* mouse (Fig. 4C, D) albeit without discernible peak. In *rd1* and *rd10* animals, the peaks in TUNEL-positive ONL cell numbers (P12 in *rd1*; P24 in *rd10*) coincided temporally with those of calpain activity and calpain-2 labelling.

AIF and caspase-3 levels argue against classical apoptosis in dying rods

How high intracellular [Ca^{2+}] and Ca^{2} dysregulation are linked to photoreceptor cell death is still unclear. Prominent candidates for Ca^{2+}-dependent downstream pathways are apoptotic cell death through caspase effectors (13) and non-apoptotic cell death involving calpain activation (10,14). To distinguish between these two proposed pathways, we used antibodies for cleaved caspase-3, a marker protein for apoptosis (42), and AIF, a marker for programmed necrosis (10,43).

AIF-positive cells were observed in the ONL of all disease models (Fig. 5A-D). Significant increases in AIF-positive cell numbers in *rd10* occurred at the same time-point (P18; for all statistics, see Supplemental Table 2) as those of TUNEL and calpain activity. In *rd1* retina, a significant increase in AIF-positive cell numbers was seen only at the P30 time-point. In addition, a small, non-significant increase in AIF-positive cells number was seen in *cpfl1* retina.

Increases in the numbers of cells showing caspase-3 activation were observed in all mouse lines (Fig. 6A-C), though to a low level (Fig. 6D) and not at all time-points (for all statistics, see Supplemental Table 2). Significantly higher numbers of caspase-3 positive cells were seen in *rd1* retina from P18 on, peaking at P24. Caspase-3 positive cells were often overlapping with cones, was marked by the TN-XL biosensor expression (29). Indeed, when we analysed for *rd1* cones expressing caspase-3, we found that at P24 a substantial number of cones were

positive for activated caspase-3 (Fig. 7A-D). This delayed caspase-3 activation is compatible with the execution of apoptosis during secondary *rd1* cone degeneration.

Spatio-temporal mapping of degenerative markers in the retina

In the experiments so far, we noticed that the distribution of data points for a certain time-point was often quite broad and featured multiple peaks (*e.g.* Fig. 2D, *rd1* at P12; Fig. 3D, *rd10* at P24). Possible explanations for this are variability between individual mice and variability of degeneration state across the retina. We tested the latter by resolving the distributions of the markers along the retina's dorso-ventral axis for all time-points and lines (Fig. 8). To this end, we collapsed data points along the naso-temporal axis, calculating the mean distribution along the dorso-ventral axis for each time-point, and visualized the whole time series as spatio-temporal heat maps (for original maps, see Supplemental Figs. 2-7).

Indeed, the spatial analysis revealed that degeneration did not occur uniformly across the retina of a given time-point: For instance, in *rd1* animals, the peak in calpain activity at P12 first occurred in the central retina and then at P14 in the peripheral retina (Supplemental Fig. 2, 2nd row). This sequence was also visible in the spatio-temporal maps of *rd1* for calpain activity, TUNEL, and calpain-2 (Fig. 8, 2nd column). A similar trend, though somewhat less clear, was observed in *rd10* retina (Fig. 8, 3rd column; Supplemental Figs. 2-7, 3rd row). Therefore, this spatial inhomogeneity of cell death markers for a given time-point at least partially explains the broad distribution of the data points (*cf*. Figs. 2-6).

Probabilistic models infer sequences of markers

When comparing the spatio-temporal heat maps for different markers, we noticed that markers within the same retinal region seemed to appear in a certain temporal sequence that differed and/or was delayed between mouse lines. For example, in *rd1* central retina, the peaks of calpain-2, calpain activity, and TUNEL staining appeared to coincide (~P12),

followed by smaller peaks of caspase-3 (P24) and AIF (P30 or later). In *rd10*, the broader "peaks" of calpain-2, calpain activity, and TUNEL also coincided, yet they were more spread out (from P18 to P30) and – as opposed to *rd1* – associated with minor elevations of AIF- and calpain-1, but less so with caspase-3.

To more quantitatively identify the time-points at which each cell death markers peaked in each mouse line, we fitted a set of probabilistic models using Gaussian processes (Fig. 9; for details, see Methods). These models infer the mean and standard deviation of the number of labelled ONL cells over time. To estimate the time at which each marker peaked, we drew 10,000 samples from the posterior of each fitted Gaussian process model and identified the maxima in each sample. The distribution of these maxima indicated the likely peak of each marker (Fig. 10). From these distributions, we identified the most likely sequences of molecular markers in each disease model with a cut-off point of 5% (Fig. 10).

The overall levels of all markers were low for wt and *cpfl1* animals, causing a relatively low level of confidence in the model predictions. In wt mice, calpain activity preceded calpain-2, followed by TUNEL and calpain-1, while in *cpfl1*, AIF was predicted to precede calpain-1 before TUNEL, calpain-2 and calpain activity. In the *rd1* situation there was more confidence in the inferred molecular sequences, showing increased calpain activity, calpain-2-, and TUNEL-positive cells to occur first in the sequence, while AIF and calpain-1 were predicted to always be the last two markers (Fig. 10A). In *rd10*, no sequence had a probability greater than 0.05 (Supplemental Fig. 8). Taken together, the GP models distinguish between the clear molecular sequences in the *rd1* compared to the more ambiguous progression in *cpfl1* and *rd10*.

Discussion

Here, we show that activation of calpain-2, but not calpain-1, is strongly correlated with photoreceptor cell death. We show that caspase-3, while not involved in primary rod photoreceptor death, may be responsible for secondary cone degeneration. Our data suggests that peaks for calpain activity, calpain-2, and TUNEL are correlated in space and time starting in the centre of the retina before spreading to the periphery following the onset of degeneration. Modelling results are consistent with the execution of two distinct cell death mechanisms in the *rd1* retina: non-apoptotic cell death during primary rod degeneration and "classical" caspase-driven apoptosis during secondary cone degeneration.

Ca^{2+} dysregulation and cell death

$[Ca^{2+}]$ dysregulation occurs in photoreceptors with *Pde6* gene mutations, typically resulting in higher Ca^{2+} concentrations (30). This rise in $[Ca^{2+}]$ would lead to increased activity of the plasma membrane NCKX, an exchanger responsible for maintaining appropriate Ca^{2+} levels in photoreceptor outer segments (44). NCKX is driven by a K^+ gradient, which in turn is maintained by Na^+/K^+-ATPases. Elsewhere in the cell, low $[Ca^{2+}]$ is ensured by specific Ca^{2+}-ATPases, which have the highest ATP affinity of all ATPases (45). This may explain why low $[Ca^{2+}]$ can be maintained even when most of the general cellular ATP has become depleted (45). As necrosis is a passive process that does not require ATP, it has long been suspected that the levels of ATP in the cell are a determining factor for whether, under stress, the cell chooses apoptosis or necrosis to complete cell death (Criddle et al., 2007; Leist et al., 1997; Tsujimoto, 1997). The high levels of Ca^{2+} needed to produce the observed calpain-2 activation could indicate that previously any remaining ATP was already used up by Ca^{2+}-ATPases. Hence, a cell death pathway not dependent on ATP (such as necrosis) would seem to be the only pathway left for the photoreceptors to avail of.

It is tempting to speculate on what could cause such a loss of ATP. A relatively straightforward explanation might be that high cGMP levels caused by *Pde6* mutations, lead

to the constitutive over-activation of CNG channels, and thus a constant need for ATP-dependent ion extrusion, which eventually overburdens the photoreceptor capacity to produce ATP.

Secondary cone death driven by apoptosis in rd1

While the majority of *rd1* rods die between P12 and P14, some cells, mostly cones, remain in the outer retina beyond P18. Interestingly, we did find that a substantial cohort of the remaining cones were also positive for caspase-3 in the *rd1* mouse at P24. This would suggest that, while the primary rod degeneration is non-apoptotic, secondary cone degeneration is, in fact, an apoptotic process. In this context, it is also notable that calpain-1 activation was seen in *rd10* retina, but not in *rd1* (or *cpfl1*). Since calpain-1 has been implicated in neuroprotective mechanisms, the remaining photoreceptors may use calpain-1 to prolong their survival (discussed in Baudry & Bi, 2016). When compared to *rd1*, the somewhat slower progression of the *rd10* degeneration may give the cells more time to activate such endogenous calpain-1 dependent protection.

Spatial occurrences of markers, and progression of cell death

Within the *rd1* mouse retina, a clear centre-to-periphery progression can be seen for calpain activity, calpain-2 up-regulation, and TUNEL staining. This suggests that the activity of calpain (likely calpain-2) drives the advance of cell death across the retina. The centre-to-periphery wave of cell death is well established and thought to follow cell maturation patterns in the *rd1* moose (49). Cell death patterns seen in the *rd10* retina are less well-known but may begin in the mid-periphery and work simultaneously towards and away from the optic nerve (50,51). In our examination of the *rd10* mouse, a centre to peripheral gradient was indeed seen for calpain activity, calpain-2, and TUNEL, although this gradient was not as distinct as that in the *rd1* mouse. This could be due to time-point selection or to the fact that the

degeneration seen in the *rd10* mouse is less synchronous than that in the *rd1* mouse. No pattern of marker up-regulation or activation was detectable in the *cpfl1* mouse model as seen in the individual heat maps (Supplemental Fig. 2-7). This is probably due to the low number of cones in the mouse retina and the stochastic nature of the cell death seen in all mouse models of retinal dystrophies (52).

Different cell death mechanisms in Pde6b mutants?

The differences seen between *rd1* and *rd10* may provide for interesting insights into the causative degeneration mechanisms. While both models show high levels of calpain activity, calpain-2, and TUNEL, at ages corresponding to the degeneration peaks (P12 and P18, respectively), there may be differences in the mode of cell death utilised by the photoreceptors. AIF and calpain-1 activation was prevalent in the ONL of the *rd10* mouse, while the *rd1* retina did not show these markers until relatively late (P24), at which point they may be located predominately to cones. This leads us to ask whether different mutations within the two models cause different pathways of cells death. This question is difficult to address at a cellular level; however, at the tissue level it is obvious that *rd1* and *rd10* mutants differ in the onset and speed of retinal degeneration, with a marked delay and slower progression in *rd10* animals. Interestingly, calpain-1 activity has been implicated in neuroprotective mechanisms (Baudry & Bi, 2016). Hence, the somewhat slower progression of *rd10* degeneration may give individual cells more time to activate endogenous calpain-1 dependent protection (as discussed above).

The *rd10* retina also displayed a more marked up-regulation of AIF compared to *rd1*. Since AIF is a mitochondrial protein, and photoreceptor mitochondria in the inner segments grow and mature with post-natal age, it is conceivable that this apparent increase in AIF is entirely due to the later onset of *rd10* degeneration. If correct, then AIF may also be associated with

rd1 degeneration, as has been suggested before (17), but would be more difficult to detect because at the onset of *rd1* degeneration its expression was much lower.

Taken together, the cell death mechanisms seen in primary rod degeneration, in both *rd1* and *rd10* retina, are clearly connected to calpain-2 activation, independent of caspase-3, and likely involve AIF release from mitochondria – hence, indicative of non-apoptotic cell death pathways. Conversely, calpain-1 activation may play a protective role, however, a role which ultimately is not strong enough to save photoreceptors from mutation-induced degeneration.

Future directions and conclusion

Here, we adopted a "standard" experimental strategy which emphasises the use of large numbers of samples at a small number of predetermined time-points (10,30). Although this approach was useful for inferring the state of the system at particular disease stages, the rigidity of the sampling came at the cost of lower temporal resolution. Where the temporal precision is critical, it would be preferable to adopt a proactive strategy, using GP models to pre-select the optimal time-points for particular hypotheses (Chaloner & Verdinelli, 1995; Lindley, 1956; Pillow, 2016). This should make it possible to infer more accurately the non-linear progression of each marker over time, with fewer samples than would be needed in a predetermined or purely random approach.

Temporal-spatial mapping of degenerative markers in the retina showed that Ca^{2+}-dependent calpain activity in hereditary retinal degeneration rises in congress with the degeneration of the tissue. The observed calpain activity was strongly correlated and likely caused by activation of calpain-2, suggesting calpain-2 as an important driver of photoreceptor cell death. We provide further strong evidence for primary rod degeneration being a non-apoptotic mechanism, even though, at least in *rd1* retina, the delayed appearance of caspase-3 activation in cones suggests apoptosis as a driver of secondary cone degeneration.

These results demonstrate the complexity of cell death mechanisms in hereditary retinal degeneration and highlight the importance of classifying the relevant cell death mechanisms, in the various stages of disease progression. Notably, the confirmation and identification of Ca^{2+}-dysregulation and calpain-2 as components of a pathway driving photoreceptor degeneration may guide the development of future therapeutics.

Figures

Figure 1. Photoreceptor degeneration-related cell loss in different mouse lines. **A-H**, representative images of sections from *wt* (A), (E), *rd1* (B), (F), *rd10* (C), (G) and *cpfl1* (D), (H) analysed with DAPI, images at P18 (top) and P30 (bottom) of each mouse line. **I**, cell loss was measured using outer nuclear layer (ONL) thickness during the first post-natal month in *rd1* (cherry), *rd10* (amber), *cpfl1* (lilac), and wild-type (wt, emerald) mice (n=3 animals per mouse line and time-point).

Figure 2. Temporal progression of calpain activity in different mouse lines. **A-C**, representative images of sections from *rd1* (A), *rd10* (B), and *cpfl1* (C) analysed with the calpain assay; each image of a mutant retina (left) is aged-matched with a wt control (right). **D**, normalised number of fluorescent cells in the ONL (per 1,000 μm^2), indicative of calpain activity in photoreceptors, as a function of age (n=45 observations obtained on 3 animals per mouse line and time-point). Statistical analysis was Kruskal–Wallis one-way analysis of variance, brackets denote statistical significance ($p < 0.001$), unless otherwise indicated (**; $p < 0.01$, *; $p<0.05$). Scale bar: A-C, 50 µm.

Figure 3. Calpain-2 becomes activated during photoreceptor degeneration. **A-C**, representative images of sections from *rd1* (A), *rd10* (B), and *cpfl1* (C) analysed for calpain-2 immunoreactivity; each image of a mutant retina (left) is aged-matched with a wt control (right). **D**, normalised number of fluorescent cells in the ONL (per 1,000 μm^2), indicative of calpain-2 immunoreactive photoreceptors, as a function of age (n=45 observations obtained on 3 animals per mouse line and time-point). Statistical analysis was Kruskal–Wallis one-way analysis of variance, brackets denote statistical significance ($p < 0.001$), unless otherwise indicated (**; $p < 0.01$). Scale bar: A-C, 50 µm

Figure 4. Temporal progression of cell death in different RD and wt mouse lines. **A-C**, representative images of sections from *rd1* (A), *rd10* (B), and *cpfl1* (C) analysed with the TUNEL assay; each image of a mutant retina (left) is aged-matched with a wt control (right). **D**, normalised number of fluorescent cells in the ONL (per 1,000 μm^2), indicative of TUNEL positivity in photoreceptors, as a function of age (n=45 observations obtained on 3 animals per mouse line and time-point). Statistical analysis was Kruskal–Wallis one-way analysis of variance, brackets denote statistical significance of *** $\leq$ 0.001 unless otherwise stated. Scale bar: A-C, 50 µm.

Figure 5. AIF immunolabeling in different RD and wt mouse lines. **A-C**, representative images of sections from *rd1* (A), *rd10* (B), and *cpfl1* (C) analysed with the AIF immunofluorescence; each image of a mutant retina (left) is aged-matched with a wt control (right). **D**, normalised number of fluorescent cells in the ONL (per 1,000 μm^2), indicative of AIF immunoreactive photoreceptors, as a function of age (n=45 observations obtained on 3 animals per mouse line and time-point). Statistical analysis was Kruskal–Wallis one-way analysis of variance, brackets denote statistical significance of*** $\leq$ 0.001 unless otherwise stated. Scale bar: A-C, 50 µm.

Figure 6. Activated caspase-3 in wt and RD mouse models. **A-C**, representative images of sections from *rd1* (A), *rd10* (B), and *cpfl1* (C) stained with an antibody against activated caspase-3; each image of a mutant retina (left) is aged-matched with a wt control (right). **D**, normalised number of fluorescent cells in the ONL (per 1,000 μm^2), indicative of photoreceptors with activated caspase-3, as a function of age (n=45 observations obtained on 3 animals per mouse line and time-point). Statistical analysis was Kruskal–Wallis one-way

analysis of variance, brackets denote statistical significance of*** ≤ 0.001 unless otherwise indicated (**; p <0.01, *; p<0.05). Scale bar: A-C, 50 µm.

Figure 7. Activated caspase-3 in degenerating cone photoreceptors. **A-D**, representative images of sections from *rd1* P24 showing DAPI (A), cones expressing the TN-XL biosensor (B), activated caspase-3 (C) and a merged imaged of cones and caspase-3 (D). **E**, normalised number of fluorescent cells in the ONL (per 100 µm), indicative of cones in the wt retina at P24 (lilac), cones not showing caspase-3 activation (green), cones positive for activated caspase-3 (caspase-3 +ve; yellow) and, rods positive for activated caspase-3 (caspase-3 +ve; red; n=45 observations obtained on 3 animals per mouse line and time-point). 778 cones that remained in the 45 images 111 of them (14%) were also positive for caspase-3. Scale bar: A-D, 50 µm.

Figure 8. Summary heat maps illustrating the spatio-temporal progression of cell death markers, with image position along the y-axis (dorso-ventral) and time along x-axis (see Methods for details and Supplemental Figures 2-7 for individual maps). Each element in the heat map is the mean value averaged over the naso-temporal axis. Colours represent number of fluorescent cells in the ONL (per 1,000 μm^2) of calpain-1, calpain-2, calpain activity, AIF, caspase-3, and TUNEL.

Figure 9. Gaussian process model for the kinetics of in cell death related processes. **A**, Parameters associated with photoreceptor cell death as measured in the ONL (per 1,000 μm^2). **B**, Gaussian Process (GP) models with radial basis function kernel and additive Gaussian noise, fitted to observations to each cross of marker and mouse line. Observations

are square root transformed prior to fitting, and after fitting are squared to return the model to its original state. 5% and 95% confidence intervals are estimated using a bootstrap of 1k posterior samples, excluding the additive likelihood noise. **C,** 100 of the 1k posterior samples from the GPs. **D,** Density of the maxima of the GP posterior samples for each marker.

Figure 10. Estimation of marker sequences, using probabilistic Gaussian Process bootstrap (A). Marker sequences from probabilistic Gaussian Process bootstrap where the probability of observing the sequence was estimated to be greater than 0.05. Probabilities estimated from 1,000 samples for each marker, in each mouse line.

Methods Figure

Methods Figure 1. Illustration of the preparation protocol. Mouse eyes were marked nasally before being enucleated, dissected, fixed, and flash frozen in liquid nitrogen before sectioning. Eyes were sectioned from the nasal side towards the temporal side along the dorso-ventral axis (**A**). Consecutive sections were kept on consecutive slides (**B**). Sections were imaged along the dorso-ventral axis at five locations: Dorsal, Dorsomedial, Medial, Ventromedial and Ventral (**C**). Images were then analysed (**D**) by measuring the whole retinal area imaged (yellow dashed line), the ONL area imaged (red dashed line) and, ONL length imaged (green dashed line) for each image. ONL width was calculated by dividing the area by the length for each image. Scale bar: 50 µm.

Supplemental Materials

Supplemental Figure 1. Calpain-1 immunolabeling in different RD and wt mouse lines. **A-C**, representative images of sections from *rd1* (A), *rd10* (B), and *cpfl1* (C) analysed with the

calpain-1 positivity; each image of a mutant retina (left) is aged-matched with a wt control (right). **D**, normalised number of fluorescent cells in the ONL (per 1,000 μm^2), indicative of calpain-1 immunoreactive photoreceptors, as a function of age. Statistical analysis was performed using Kruskal–Wallis one-way analysis of variance, brackets denote statistical significance of*** $\leq$ 0.001 unless otherwise stated. Scale bar: A-C, 50 µm

Supplemental Figure 2. Heat maps for the spatio-temporal progression of calpain activity across the retina and for different mouse lines. Each map represents a time-point, the grey disk the position of the optic nerve head (map origin). Each box in a map measures 1,000 µm by 400 µm, with the colour encoding the average number of fluorescent cells in the ONL (per 1,000 μm^2). Grey areas denote areas that were not examined.

Supplemental Figure 3. Heat maps for the spatio-temporal progression of cell death (TUNEL) across the retina and for different mouse lines. Each map represents a time-point, the grey disk the position of the optic nerve head (map origin). Each box in a map measures 1,000µm by 400 µm, with the colour encoding the average number of TUNEL positive cells in the ONL (per 1,000 μm^2). Grey areas denote areas that were not examined.

Supplemental Figure 4. Heat maps for the spatio-temporal progression of calpain-2 activity across the retina and for different mouse lines. Each map represents a time-point, the grey disk the position of the optic nerve head (map origin). Each box in a map measures 1,000 µm by 400 µm, with the colour encoding the average number of fluorescent cells in the ONL (per 1,000 μm^2). Grey areas denote areas that were not examined.

Supplemental Figure 5. Heat maps for the spatio-temporal progression of AIF activity across the retina and for different mouse lines. Each map represents a time-point, the grey disk the position of the optic nerve head (map origin). Each box in a map measures 1,000 µm by 400 µm, with the colour encoding the average number of fluorescent cells in the ONL (per 1,000 μm^2). Grey areas denote areas that were not examined.

Supplemental Figure 6. Heat maps for the spatio-temporal progression of calpain-1 across the retina and for different mouse lines. Each map represents a time-point, the grey disk the position of the optic nerve head (map origin). Each box in a map measures 1,000 µm by 400 µm, with the colour encoding the average number of fluorescent cells in the ONL (per 1,000 μm^2). Grey areas denote areas that were not examined.

Supplemental Figure 7. Heat maps for the spatio-temporal progression of caspase-3 activity across the retina and for different mouse lines. Each map represents a time-point, the grey disk the position of the optic nerve head (map origin). Each box in a map measures 1,000 µm by 400 µm, with the colour encoding the average number of fluorescent cells in the ONL (per 1,000 μm^2). Grey areas denote areas that were not examined.

Supplemental Figure 8. Sequence is defined to be the expected order of the peaks for each marker from probabilistic Gaussian Process bootstrap.

Supplemental Tables

calpain activity

	wt		*rd1*		*rd10*		*cpfl1*	
	Mice	Images	Mice	Images	Mice	Images	Mice	Images
P10	3	45	3	45	-	-	-	-
P12	3	44	3	45	-	-	-	-
P14	3	44	3	50	5	75	3	55
P18	3	45	3	41	4	74	3	54
P24	3	39	6	76	3	50	3	45
P30	3	45	3	40	3	45	3	45
P60	3	44	-	-	-	-	3	43
P90	3	32	-	-	-	-	3	45
P120	3	45	-	-	-	-	3	45
calpain-2								
P10	3	45	3	45	-	-	-	-
P12	3	45	3	45	-	-	-	-
P14	3	45	3	44	3	45	3	45
P18	3	45	3	45	3	44	3	45
P24	3	45	3	45	3	45	3	45
P30	3	45	3	45	3	45	3	45
TUNEL								
P10	3	45	3	45	-	-	-	-
P12	3	45	3	45	-	-	-	-
P14	3	45	3	45	3	45	3	45
P18	3	45	3	45	3	45	3	45
P24	3	45	3	45	3	45	3	45
P30	3	45	3	45	3	45	3	45
AIF								
P10	3	45	3	45	-	-	-	-
P12	3	45	3	45	-	-	-	-
P14	3	44	3	40	3	45	3	45
P18	3	45	3	45	3	45	3	44
P24	3	45	3	45	3	45	3	45
P30	3	45	3	45	3	45	3	45

caspase-3								
P10	3	45	3	45	-	-	-	-
P12	3	45	3	45	-	-	-	-
P14	3	44	3	40	3	45	3	45
P18	2	30	3	45	3	45	3	45
P24	3	45	3	45	3	45	3	45
P30	3	45	3	45	3	45	3	45
calpain-1								
P10	3	32	3	45	-	-	-	-
P12	3	39	3	44	-	-	-	-
P14	1	12	3	44	3	45	3	45
P18	3	45	3	45	3	45	3	45
P24	3	45	3	45	3	45	3	45
P30	3	45	3	45	3	45	3	45

Supplemental Table 1. Number of mice used for each marker and number of images recorded. The table gives the information for all markers used, namely, calpain activity, calpain-1, calpain-2, TUNEL, caspase-3, AIF.

calpain activity				
	Wild type	*rd1*	*rd10*	*cpfl1*
P10	0.14±0.023	0.78±0.068	-	-
P12	0.055±0.012	4.3±0.27	-	-
P14	0.053±0.0074	2.69±0.11	0.11±0.019	0.09±0.008
P18	0.051±0.0057	1.19±0.13	1.36±0.145	0.08±0.01
P24	0.0255±0.006	1.001±0.13	0.878±0.122	0.15±0.01
P30	0.06±0.02	0.74±0.12	0.82±0.068	0.12±0.01
P60	0.044±0.005	-	-	0.22±0.02
P90	0.054±0.007	-	-	0.176±0.02
P120	0.058±0.008	-	-	0.21±0.016
TUNEL				
P10	0.046±0.01	1.15±0.116	-	-
P12	0.078±0.016	6.1±0.42	-	-
P14	0.156±0.011	3.63±0.18	0.17±0.12	0.16±0.017
P18	0.14±0.011	2.94±0.3	1.76±0.23	0.21±0.019
P24	0.086±0.013	1.44±0.14	2.7±0.16	0.19±0.01
P30	0.03±0.0088	1.40±0.101	1.08±0.08	0.1±0.02
calpain-2				
P10	0.034±0.006	0.46±0.05	-	-
P12	0±0.006	0.95±0.14	-	-
P14	0.026±0.006	1.10±0.13	0±0.01	0.016±0.0049
P18	0.019±0.005	0.3±0.033	0.41±0.09	0±0.003
P24	0±0.007	0.26±0.07	0.29±0.05	0.024±0.0038
P30	0±0.003	0.19±0.088	0.73±0.1	0±0.004
calpain-1				
P10	0±0	0±0	-	-
P12	0±0.0035	0±0.0015	-	-
P14	0±0	0±0.002	0±0.002	0±0.0007
P18	0±0.0007	0±0.0016	0±0.04	0±0.002
P24	0±0.0004	0±0.004	0±0.025	0±0.0009
P30	0±0.002	0±0.014	0.38±0.05	0±0.0009
caspase-3				

P10	0±0.00095	0±0	-	-
P12	0±0.00057	0±0	-	-
P14	0±0	0±0.004	0±0	0±0.0009
P18	0±0	0±0.019	0±0.006	0±0.0004
P24	0±0	0±0.045	0±0.007	0±0
P30	0±0	0±0.008	0±0.001	0±0.0004
AIF				
P10	0±0.0006	0±0.002	-	-
P12	0±0.001	0±0.0025	-	-
P14	0±0.003	0±0.0035	0±0.003	0±0.004
P18	0±0.001	0±0.018	0.45±0.1	0±0.004
P24	0±0.0007	0±0.027	0.91±0.091	0±0.0003
P30	0±0.0023	0±0.085	0.65±0.08	0±0.0008

Supplemental Table 2: Values and statistics from each marker recorded. Median values plus/minus the standard error of the mean recorded from each mouse model at each time-point and for each marker.

References

1. Bertelsen M, Jensen H, Bregnhøj JF, Rosenberg T. Prevalence of generalized retinal dystrophy in Denmark. Ophthalmic Epidemiol. 2014;21(4):217–23.

2. Hartong DT, Berson EL, Dryja TP. Retinitis pigmentosa. Lancet. 2006;368(9549):1795–809.

3. Remmer MH, Rastogi N, Ranka MP, Ceisler EJ. Achromatopsia: a review. Curr Opin Ophthalmol. 2015;26(5).

4. Hamel C. Retinitis pigmentosa. Orphanet J Rare Dis. 2006;1(1):40.

5. DANCIGER M, BLANEY J, GAO YQ, ZHAO DY, HECKENLIVELY JR, JACOBSON SG, et al. Mutations in the PDE6B Gene in Autosomal Recessive Retinitis Pigmentosa. Genomics [Internet]. 1995;30(1):1–7. Available from: http://www.sciencedirect.com/science/article/pii/S0888754385700018

6. McLaughlin ME, Sandberg MA, Berson EL, Dryja TP. Recessive mutations in the gene encoding the β–subunit of rod phosphodiesterase in patients with retinitis pigmentosa. Nat Genet. 1993;4(2):130.

7. Sundaram V, Wilde C, Aboshiha J, Cowing J, Han C, Langlo CS, et al. Retinal structure and function in achromatopsia: implications for gene therapy. Ophthalmology. 2014;121(1):234–45.

8. Thiadens AAHJ, den Hollander AI, Roosing S, Nabuurs SB, Zekveld-Vroon RC, Collin RWJ, et al. Homozygosity mapping reveals PDE6C mutations in patients with early-onset cone photoreceptor disorders. Am J Hum Genet. 2009;85(2):240–7.

9. Kohl S, Coppieters F, Meire F, Schaich S, Roosing S, Brennenstuhl C, et al. A nonsense mutation in PDE6H causes autosomal-recessive incomplete achromatopsia.

Am J Hum Genet. 2012;91(3):527–32.

10. Arango-Gonzalez B, Trifunović D, Sahaboglu A, Kranz K, Michalakis S, Farinelli P, et al. Identification of a common non-apoptotic cell death mechanism in hereditary retinal degeneration. PLoS One. 2014;9(11):e112142.

11. Michalakis S, Becirovic E, Biel M. Retinal cyclic nucleotide-gated channels: from pathophysiology to therapy. Int J Mol Sci. 2018;19(3):749.

12. Krizaj D, Copenhagen DR. Calcium regulation in photoreceptors. Front Biosci a J virtual Libr. 2002;7:d2023.

13. Orrenius S, Zhihotovsky B, Nicotera P. Regulation of cell death: the calcium-apoptosis link. Nature Rev Cell Biol 2003; 4: 552-65. 2003.

14. Doonan F, Donovan M, Cotter TG. Activation of multiple pathways during photoreceptor apoptosis in the rd mouse. Invest Ophthalmol Vis Sci. 2005;46(10):3530–8.

15. Shang L, Huang J-F, Ding W, Chen S, Xue L-X, Ma R-F, et al. Calpain: a molecule to induce AIF-mediated necroptosis in RGC-5 following elevated hydrostatic pressure. BMC Neurosci. 2014;15(1):63.

16. Bano D, Prehn JHM. Apoptosis-Inducing Factor (AIF) in Physiology and Disease: The Tale of a Repented Natural Born Killer. EBioMedicine. 2018;

17. Sanges D, Comitato A, Tammaro R, Marigo V. Apoptosis in retinal degeneration involves cross-talk between apoptosis-inducing factor (AIF) and caspase-12 and is blocked by calpain inhibitors. Proc Natl Acad Sci. 2006;103(46):17366–71.

18. Nemova NN, Lysenko LA, Kantserova NP. Proteases of the calpain family: Structure and functions. Russ J Dev Biol [Internet]. 2010;41(5):318–25. Available from:

https://doi.org/10.1134/S1062360410050073

19. Suzuki K, Hata S, Kawabata Y, Sorimachi H. Structure, activation, and biology of calpain. Diabetes. 2004;53(suppl 1):S12–8.

20. Baudry M, Bi X. Calpain-1 and calpain-2: the yin and yang of synaptic plasticity and neurodegeneration. Trends Neurosci. 2016;39(4):235–45.

21. Khorchid A, Ikura M. How calpain is activated by calcium. Nat Struct Mol Biol. 2002;9(4):239.

22. Liu X, Van Vleet T, Schnellmann RG. The role of calpain in oncotic cell death. Annu Rev Pharmacol Toxicol. 2004;44:349–70.

23. Rizzuto R, Pinton P, Ferrari D, Chami M, Szabadkai G, Magalhaes PJ, et al. Calcium and apoptosis: facts and hypotheses. Oncogene. 2003;22(53):8619.

24. Chang B, Grau T, Dangel S, Hurd R, Jurklies B, Sener EC, et al. A homologous genetic basis of the murine cpfl1 mutant and human achromatopsia linked to mutations in the PDE6C gene. Proc Natl Acad Sci. 2009;106(46):19581–6.

25. KEELER C. Retinal degeneration in the mouse is rodless retina. J Hered. 1966;57(2):47–50.

26. Chang B, Hawes NL, Hurd RE, Davisson MT, Nusinowitz S, Heckenlively JR. Retinal degeneration mutants in the mouse. Vision Res. 2002;42(4):517–25.

27. Sancho-Pelluz J, Arango-Gonzalez B, Kustermann S, Romero FJ, van Veen T, Zrenner E, et al. Photoreceptor cell death mechanisms in inherited retinal degeneration. Mol Neurobiol. 2008;38(3):253–69.

28. Mank M, Reiff DF, Heim N, Friedrich MW, Borst A, Griesbeck O. A FRET-based calcium biosensor with fast signal kinetics and high fluorescence change. Biophys J.

2006;90(5):1790–6.

29. Wei T, Schubert T, Paquet-Durand F, Tanimoto N, Chang L, Koeppen K, et al. Light-driven calcium signals in mouse cone photoreceptors. J Neurosci. 2012;32(20):6981–94.

30. Kulkarni M, Trifunović D, Schubert T, Euler T, Paquet-Durand F. Calcium dynamics change in degenerating cone photoreceptors. Hum Mol Genet. 2016;25(17):3729–40.

31. Paquet Durand F, Azadi S, Hauck SM, Ueffing M, van Veen T, Ekström P. Calpain is activated in degenerating photoreceptors in the rd1 mouse. J Neurochem. 2006;96(3):802–14.

32. Williams CK, Rasmussen CE. Gaussian processes for machine learning. MIT Press. 2006;2(3):4.

33. GPy. GPy: A gaussian process framework in python [Internet]. GPy: A gaussian process framework in phython. 2014. p. http://github.com/SheffieldML/GPy. Available from: http://github.com/SheffieldML/GPy

34. Jeon C-J, Strettoi E, Masland RH. The major cell populations of the mouse retina. J Neurosci. 1998;18(21):8936–46.

35. Behrens C, Schubert T, Haverkamp S, Euler T, Berens P. Connectivity map of bipolar cells and photoreceptors in the mouse retina. Elife. 2016;5:e20041.

36. Croall DE, Ersfeld K. The calpains: modular designs and functional diversity. Genome Biol. 2007;8(6):218.

37. Goll DE, Thompson VF, Li H, Wei WEI, Cong J. The calpain system. Physiol Rev. 2003;83(3):731–801.

38. Goñi-Oliver P, Lucas JJ, Avila J, Hernández F. N-terminal Cleavage of GSK-3 by

Calpain a new form of GSK-3 regulation. J Biol Chem. 2007;282(31):22406–13.

39. Chen LY, Rex CS, Casale MS, Gall CM, Lynch G. Changes in synaptic morphology accompany actin signaling during LTP. J Neurosci. 2007;27(20):5363–72.

40. Goll DE. Properties and biological regulation of the calpain system. Expr tissue proteinases Regul protein Degrad as Relat to meat Qual. 1995;47–68.

41. Kraupp BG, Ruttkay□Nedecky B, Koudelka H, Bukowska K, Bursch W, Schulte□Hermann R. In situ detection of fragmented DNA (TUNEL assay) fails to discriminate among apoptosis, necrosis, and autolytic cell death: a cautionary note. Hepatology. 1995;21(5):1465–8.

42. Mazumder S, Plesca D, Almasan A. Caspase-3 activation is a critical determinant of genotoxic stress-induced apoptosis. In: Apoptosis and Cancer. Springer; 2008. p. 13–21.

43. Wang S, Liao L, Wang M, Zhou H, Huang Y, Wang Z, et al. Pin1 promotes regulated necrosis induced by glutamate in rat retinal neurons via CAST/Calpain2 pathway. Front Cell Neurosci. 2018;11:425.

44. Jensen TP, Buckby LE, Empson RM. Expression of plasma membrane Ca2+ ATPase family members and associated synaptic proteins in acute and cultured organotypic hippocampal slices from rat. Dev brain Res. 2004;152(2):129–36.

45. Bruce JIE. Metabolic regulation of the PMCA: role in cell death and survival. Cell Calcium. 2017;

46. Criddle DN, Gerasimenko JV, Baumgartner HK, Jaffar M, Voronina S, Sutton R, et al. Calcium signalling and pancreatic cell death: apoptosis or necrosis? Cell Death Differ. 2007;14(7):1285.

47. Leist M, Single B, Castoldi AF, Kühnle S, Nicotera P. Intracellular adenosine triphosphate (ATP) concentration: a switch in the decision between apoptosis and necrosis. J Exp Med. 1997;185(8):1481–6.

48. Tsujimoto Y. Apoptosis and necrosis: intracellular ATP level as a determinant for cell death modes. Cell Death Differ. 1997;4(6):429.

49. Noell WK. Studies on visual cell viability and differentiation. Ann N Y Acad Sci. 1958;74(1):337–61.

50. Barhoum R, Martinez-Navarrete G, Corrochano S, Germain F, Fernández-Sánchez L, De la Rosa EJ, et al. Functional and structural modifications during retinal degeneration in the rd10 mouse. Neuroscience. 2008;155(3):698–713.

51. Strettoi E, Pignatelli V. Modifications of retinal neurons in a mouse model of retinitis pigmentosa. Proc Natl Acad Sci. 2000;97(20):11020–5.

52. Clarke G, Collins RA, Leavitt BR, Andrews DF, Hayden MR, Lumsden CJ, et al. A one-hit model of cell death in inherited neuronal degenerations. Nature. 2000;406(6792):195.

53. Lindley D V. On a Measure of the Information Provided by an Experiment. Ann Math Stat [Internet]. 1956;27(4):986–1005. Available from: http://www.jstor.org/stable/2237191

54. Chaloner K, Verdinelli I. Bayesian experimental design: A review. Stat Sci. 1995;273–304.

55. Pillow, J.W. PM. Adaptive Bayesian methods for closed-loop neurophysiology. In: Closed Loop Neuroscience. 2016.

Acknowledgements:

We thank Sylvia Bolz, Norman Rieger, and Gordon Eske for technical support and guidance. We also thank Philipp Hennig for commentary and feedback on the GP modelling. This study was supported by the German Research Foundation (DFG; EU42/8-1, PA1751/7-1, TEBE5601/4-1, EXC 307, EXC2064) and the German Ministry of Education and Research (BMBF; FKZ 01GQ1601).

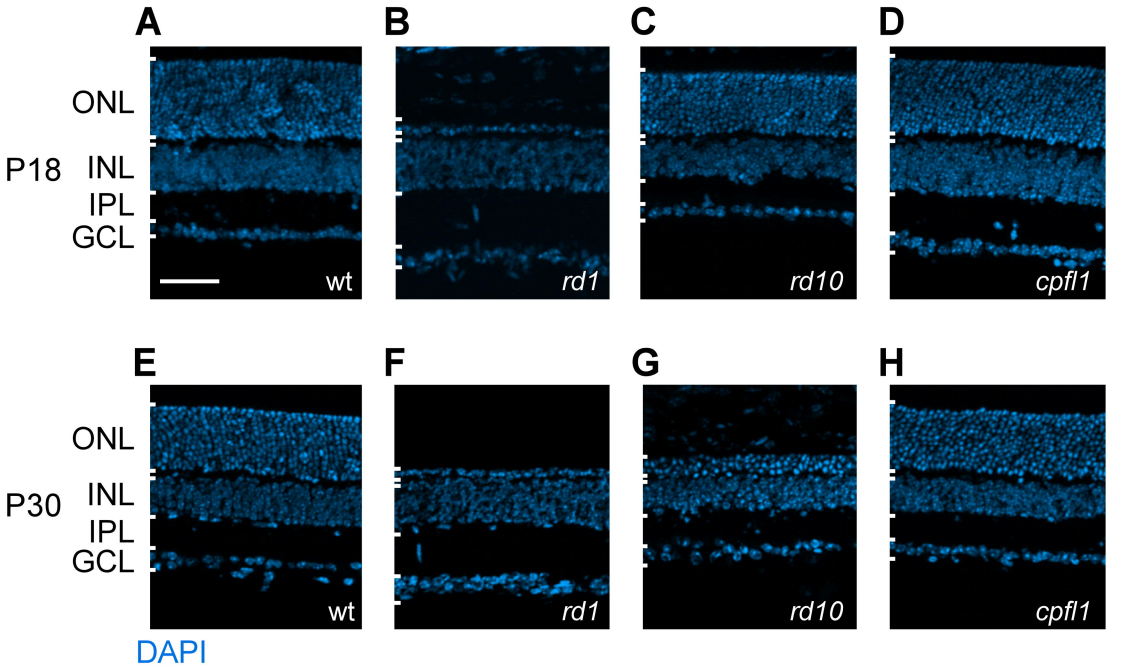
A
B
C
D
ONL
P18
INL
IPL
GCL
wt
rd1
rd10
cpfl1
E
F
G
H
ONL
P30
INL
IPL
GCL
wt
rd1
rd10
cpfl1
DAPI

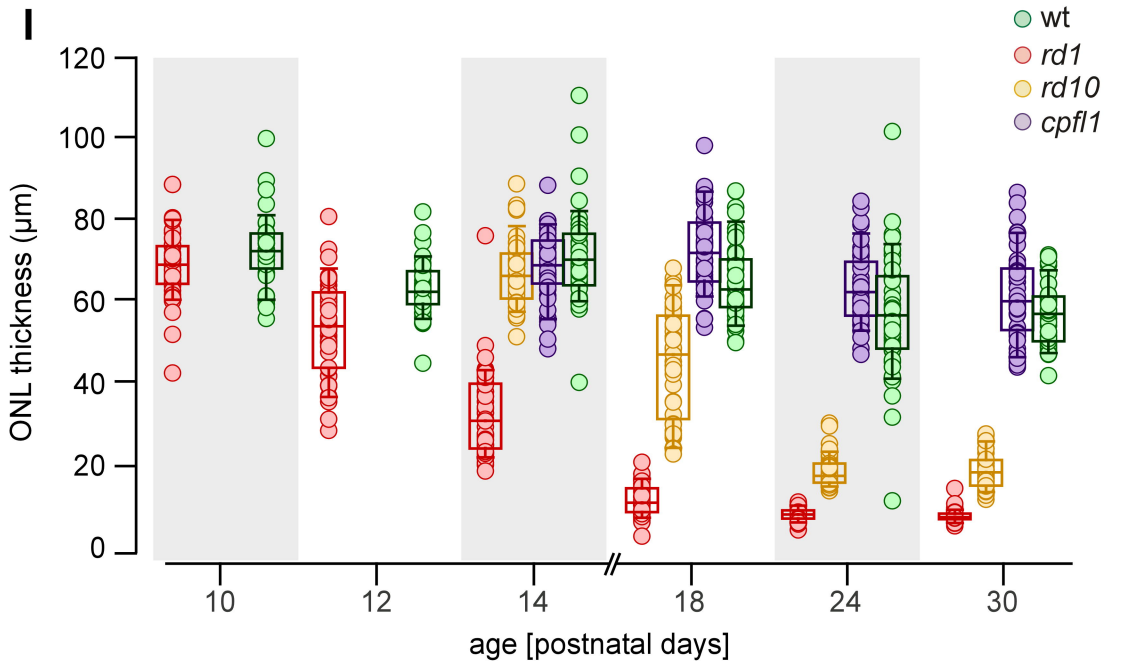
I
wt
rd1
rd10
cpfl1
ONL thickness (µm)
120
100
80
60
40
20
0
10
12
14
18
24
30
age [postnatal days]

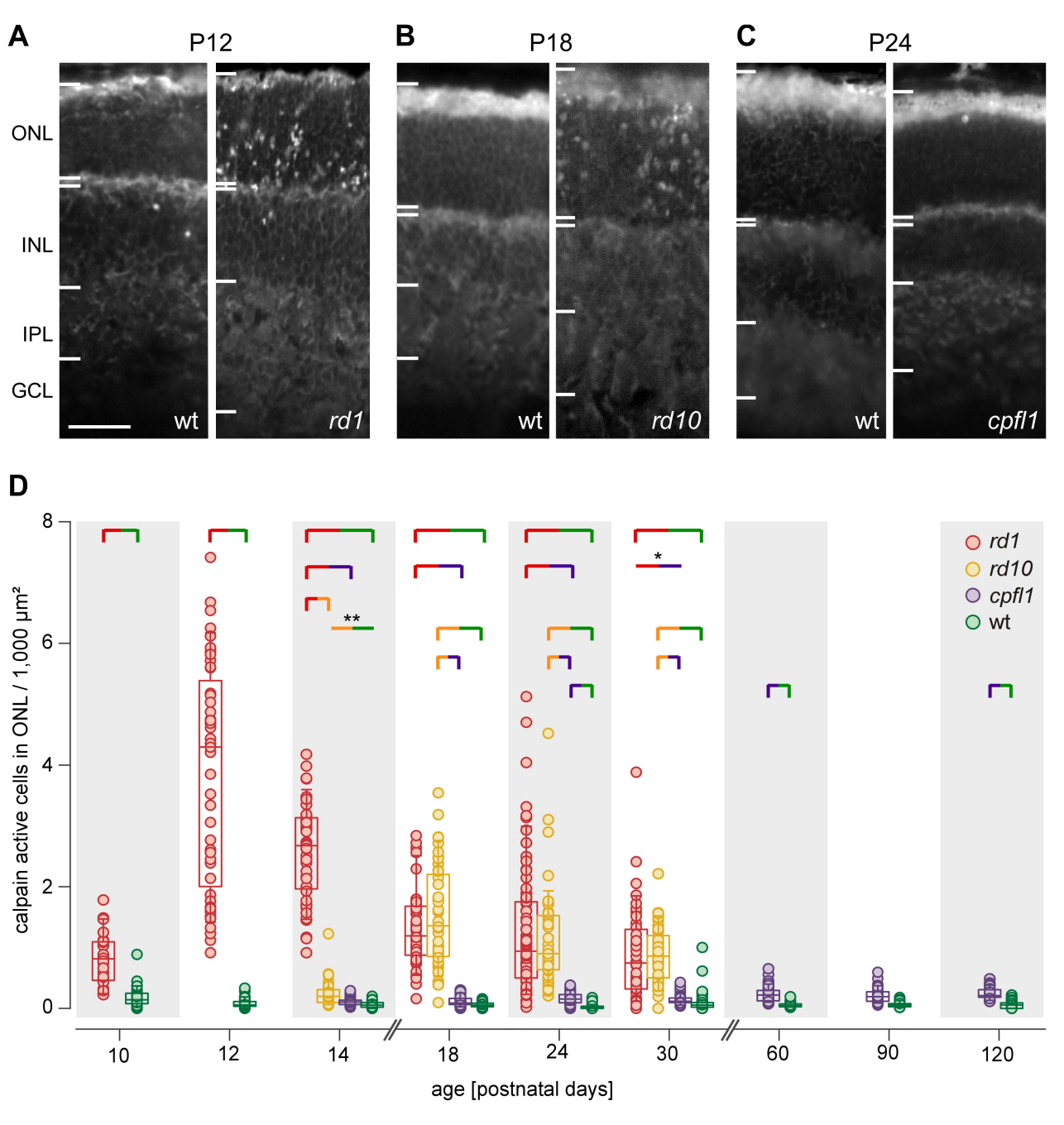
A
P12
ONL
INL
IPL
GCL
wt
rd1
B
P18
wt
rd10
C
P24
wt
cpfl1
D
calpain active cells in ONL / 1,000 µm²
0
2
4
6
8
**
*
rd1
rd10
cpfl1
wt
10
12
14
18
24
30
60
90
120
age [postnatal days]

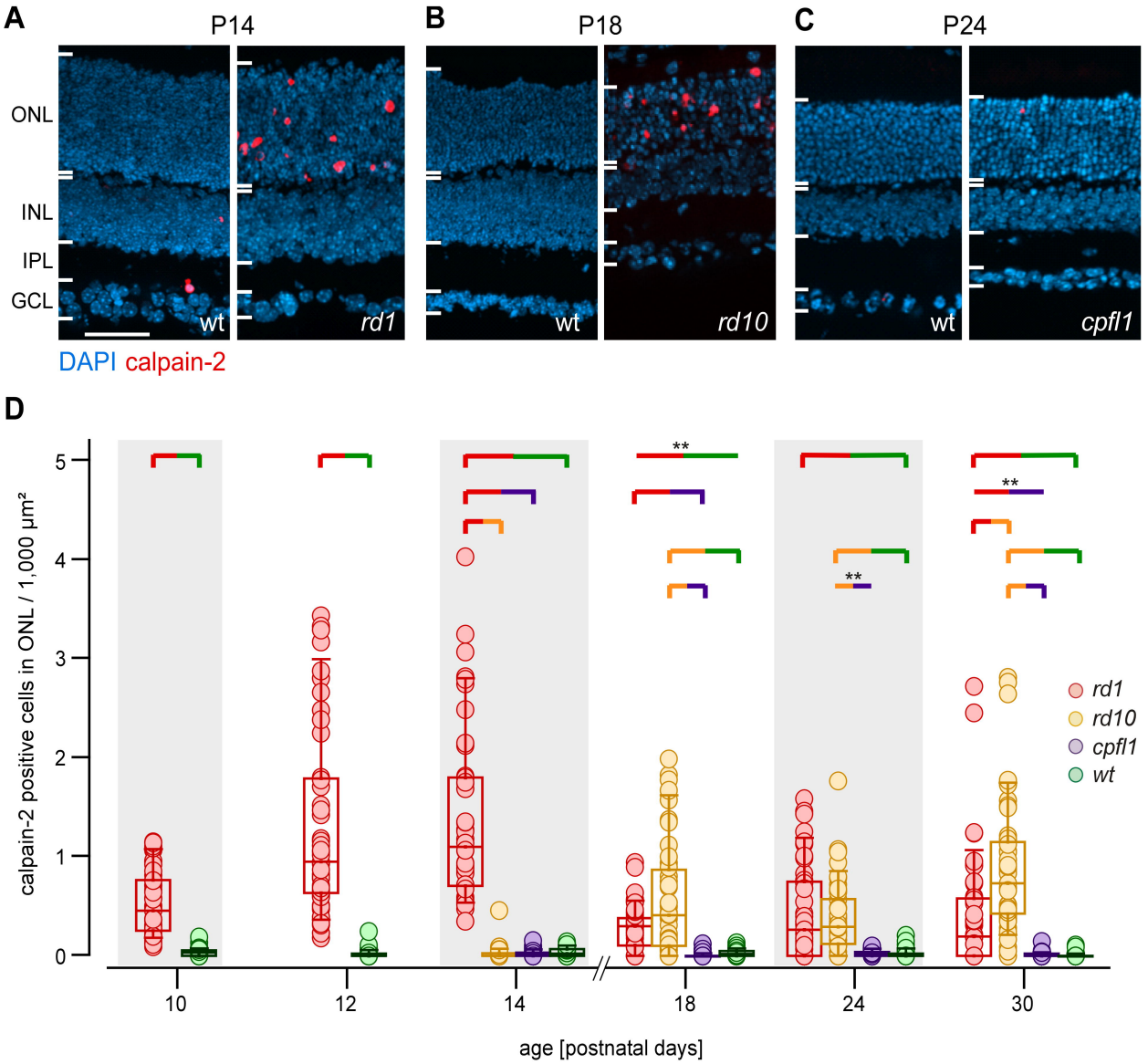
A
P14
B
P18
C
P24
ONL
INL
IPL
GCL
wt
rd1
wt
rd10
wt
cpfl1
DAPI calpain-2
D
calpain-2 positive cells in ONL / 1,000 µm²
0
1
2
3
4
5
**
**
**
rd1
rd10
cpfl1
wt
10
12
14
18
24
30
age [postnatal days]

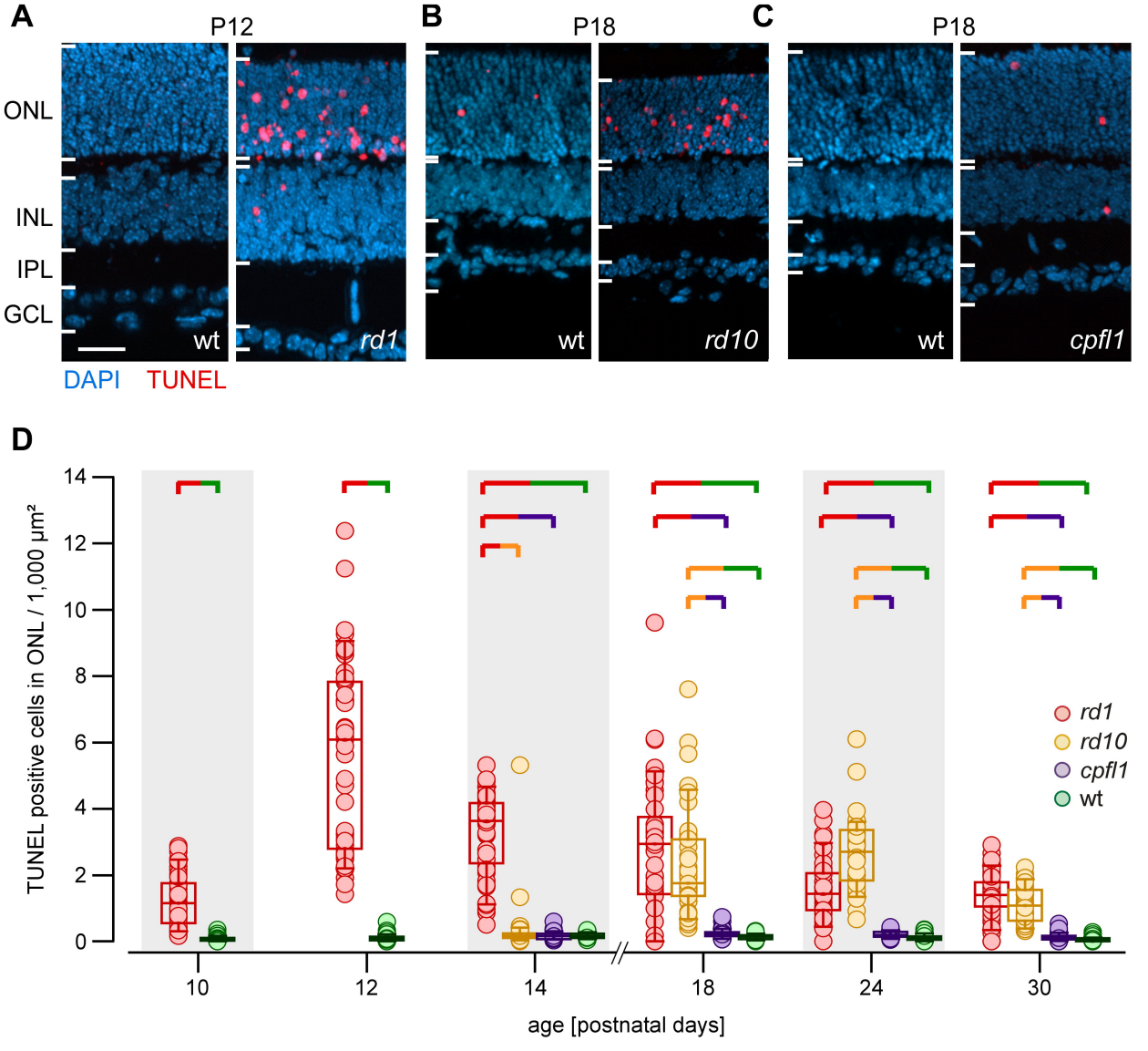
A
P12
B
P18
C
P18
ONL
INL
IPL
GCL
wt
rd1
wt
rd10
wt
cpfl1
DAPI
TUNEL
D
TUNEL positive cells in ONL / 1,000 µm²
0
2
4
6
8
10
12
14
10
12
14
18
24
30
age [postnatal days]
rd1
rd10
cpfl1
wt

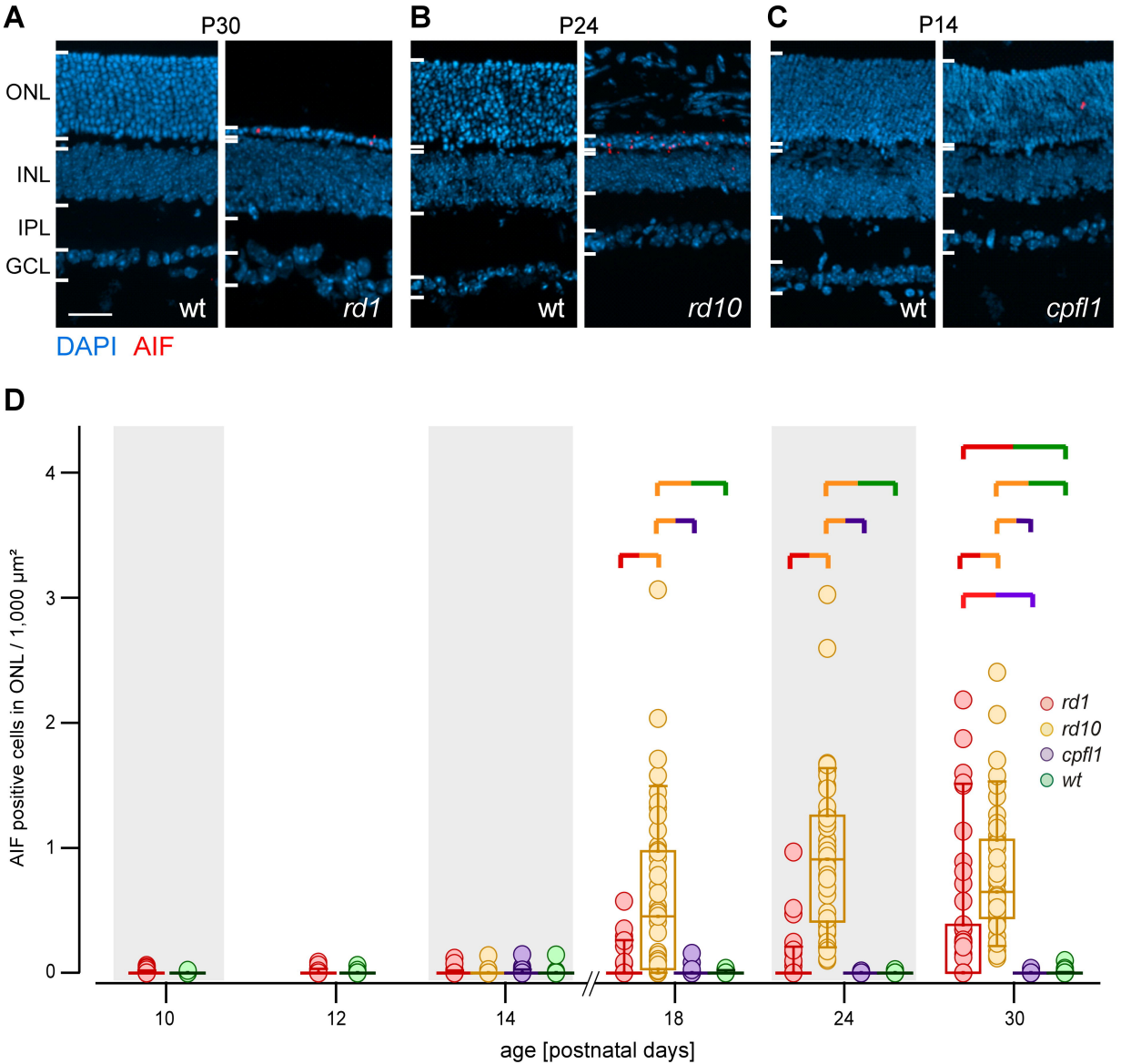
A
P30
B
P24
C
P14
ONL
INL
IPL
GCL
wt
rd1
wt
rd10
wt
cpfl1
DAPI AIF
D
AIF positive cells in ONL / 1,000 µm²
0
1
2
3
4
10
12
14
18
24
30
age [postnatal days]
rd1
rd10
cpfl1
wt

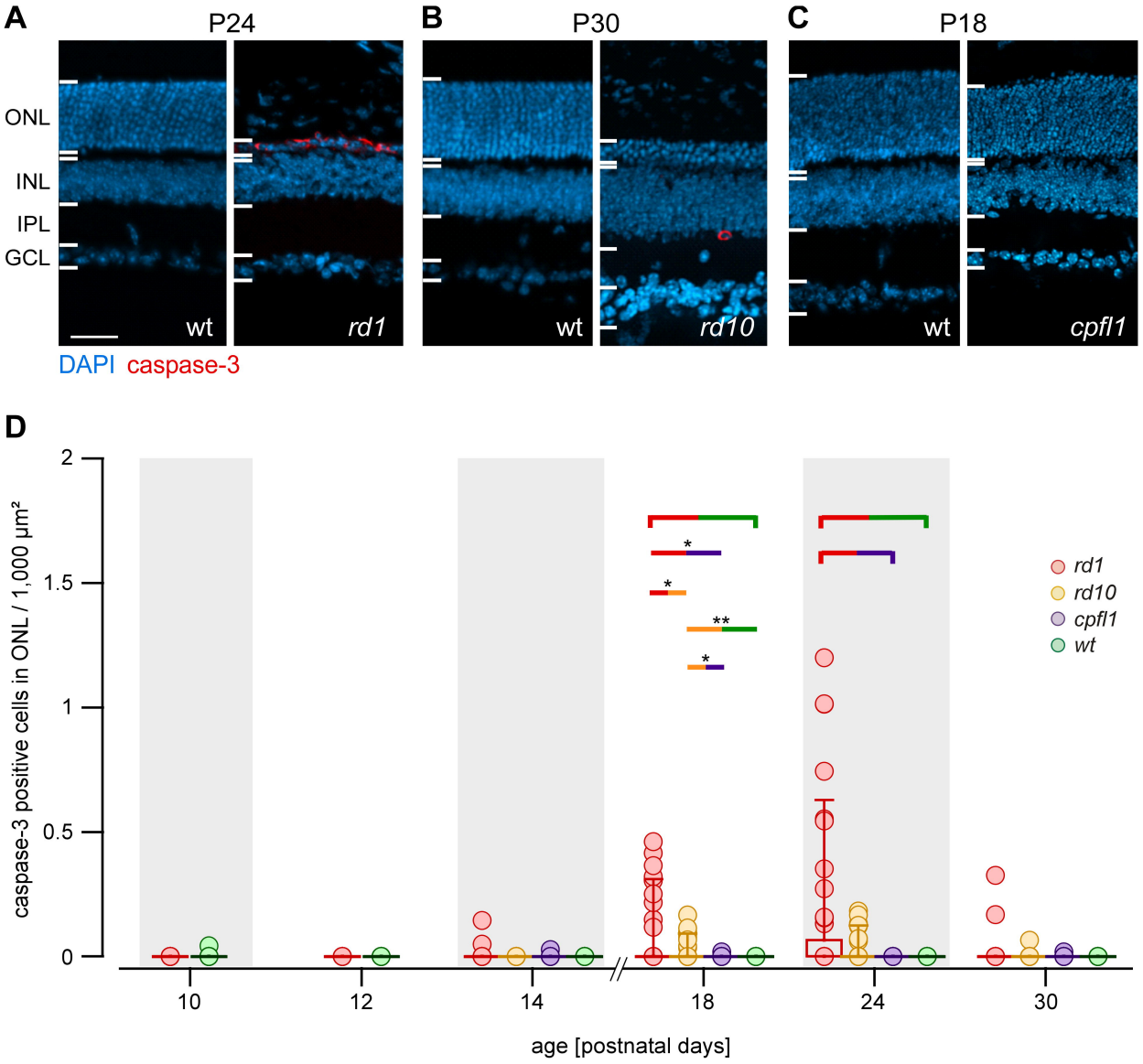
A
P24
B
P30
C
P18
ONL
INL
IPL
GCL
wt
rd1
wt
rd10
wt
cpfl1
DAPI caspase-3
D
caspase-3 positive cells in ONL / 1,000 µm²
2
1.5
1
0.5
0
10
12
14
18
24
30
age [postnatal days]
rd1
rd10
cpfl1
wt
*
*
**
*

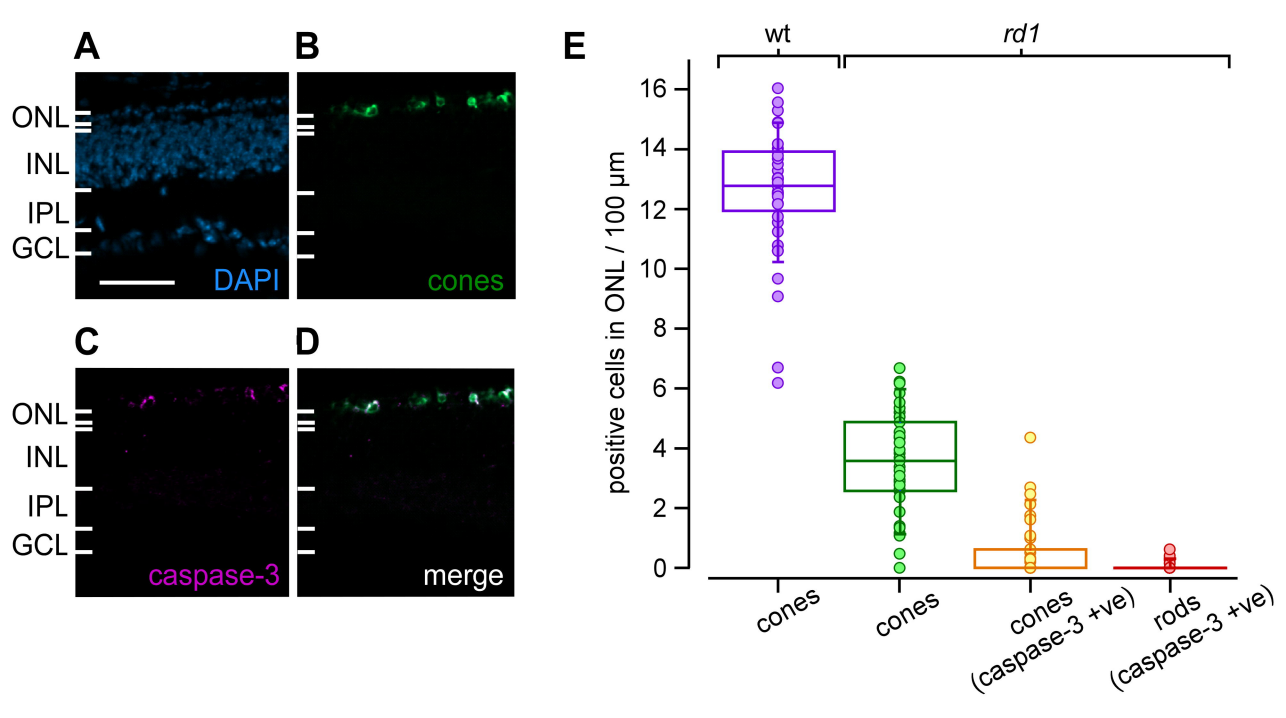
A
B
C
D
E
ONL
INL
IPL
GCL
DAPI
cones
caspase-3
merge
wt
rd1
positive cells in ONL / 100 µm
0
2
4
6
8
10
12
14
16
cones
cones
cones (caspase-3 +ve)
rods (caspase-3 +ve)

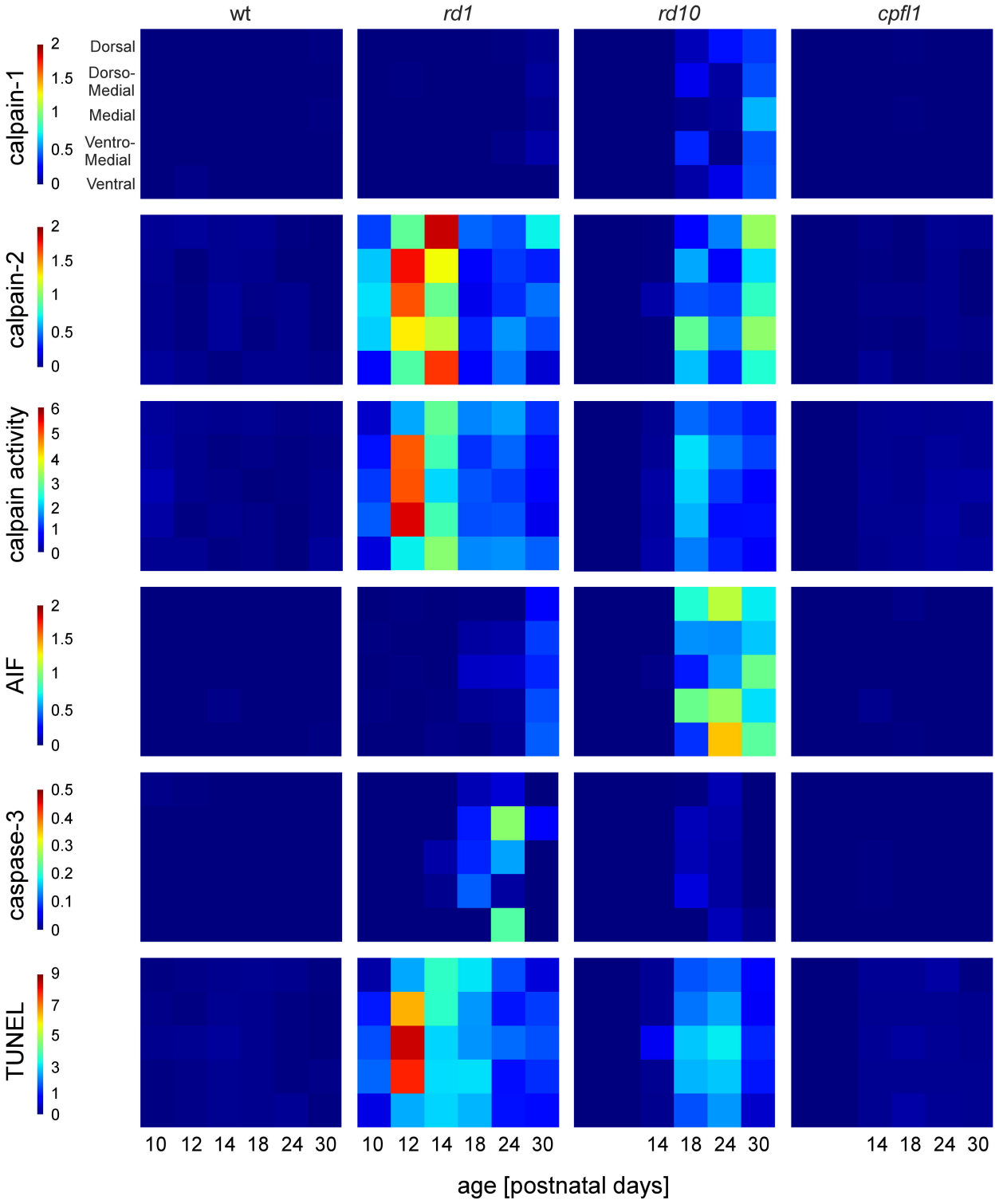
wt
rd1
rd10
cpfl1
calpain-1
calpain-2
calpain activity
AIF
caspase-3
TUNEL
Dorsal
Dorso-Medial
Medial
Ventro-Medial
Ventral
10 12 14 18 24 30
14 18 24 30
age [postnatal days]

A
B
C
D
wt
rd1
rd10
cpfl1
AIF
calpain-1
calpain-2
calpain activty
caspase-3
TUNEL
markers in ONL
peak of marker in ONL
age [postnatal days]

wt	Probability						
	0.1478	AIF	calpain	caspase-3	Calpain-2	TUNEL	calpain-1
	0.1101	AIF	calpain	calpain-2	TUNEL	caspase-3	calpain-1
	0.1071	calpain	caspase-3	calpain-2	TUNEL	AIF	calpain-1
	0.0853	calpain	calpain-2	TUNEL	caspase-3	AIF	calpain-1
	0.0625	AIF	calpain	calpain-2	caspase-3	TUNEL	calpain-1
	0.0563	calpain	caspase-3	calpain-2	TUNEL	calpain-1	AIF
rd1							
	0.264	TUNEL	calpain	calpain-2	caspase-3	AIF	calpain-1
	0.1489	calpain	TUNEL	calpain-2	caspase-3	AIF	calpain-1
	0.0935	calpain	calpain-2	TUNEL	caspase-3	AIF	calpain-1
	0.0856	TUNEL	calpain	calpain-2	caspase-3	calpain-1	AIF
	0.0705	calpain	calpain-2	caspase-3	TUNEL	AIF	calpain-1
	0.0695	TUNEL	calpain-2	calpain	caspase-3	AIF	calpain-1
	0.0511	calpain	calpain-2	caspase-3	calpain	AIF	calpain-1
cpfl1							
	0.1701	AIF	calpain-1	TUNEL	calpain-2	calpain	caspase-3
	0.1032	caspase-3	AIF	calpain-1	TUNEL	calpain-2	calpain
	0.0718	AIF	caspase-3	calpain-1	TUNEL	calpain-2	calpain
	0.0518	AIF	calpain-2	calpain-1	TUNEL	calpain	caspase-3

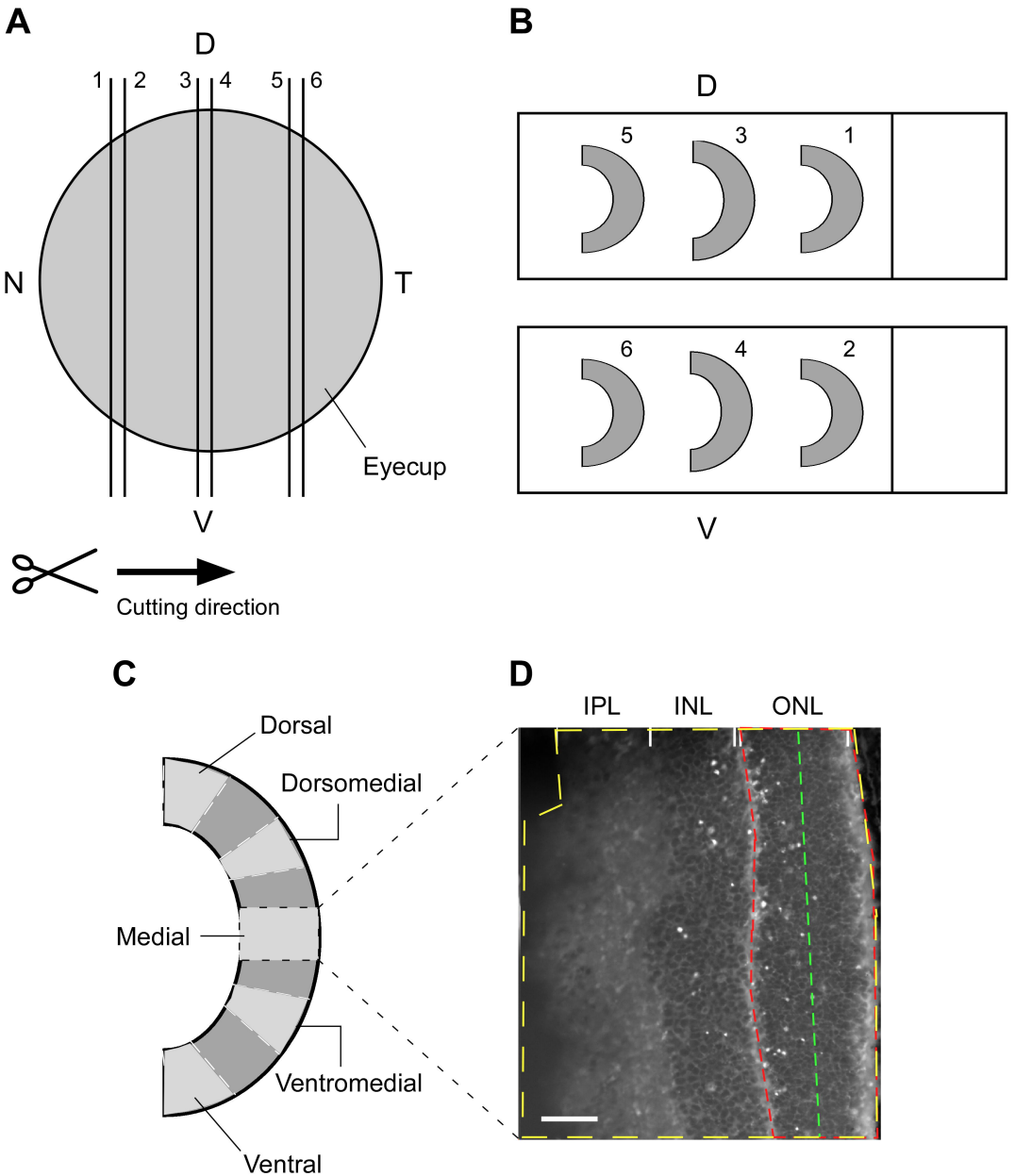
A
D
1
2
3
4
5
6
N
T
Eyecup
V
Cutting direction
B
D
5
3
1
6
4
2
V
C
Dorsal
Dorsomedial
Medial
Ventromedial
Ventral
D
IPL
INL
ONL

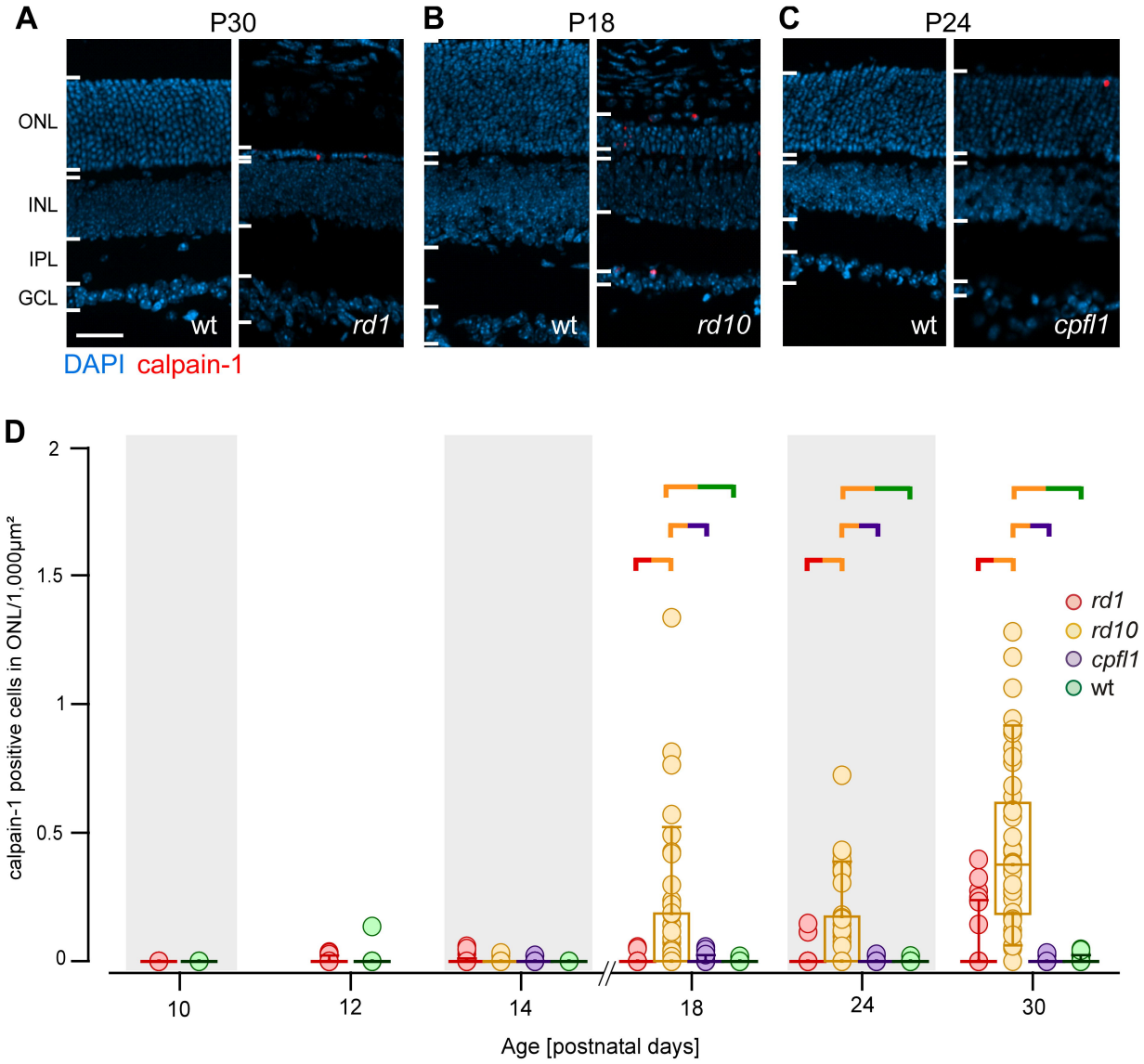
A
P30
B
P18
C
P24
ONL
INL
IPL
GCL
wt
rd1
wt
rd10
wt
cpfl1
DAPI calpain-1
D
calpain-1 positive cells in ONL/1,000µm²
2
1.5
1
0.5
0
10
12
14
18
24
30
Age [postnatal days]
rd1
rd10
cpfl1
wt

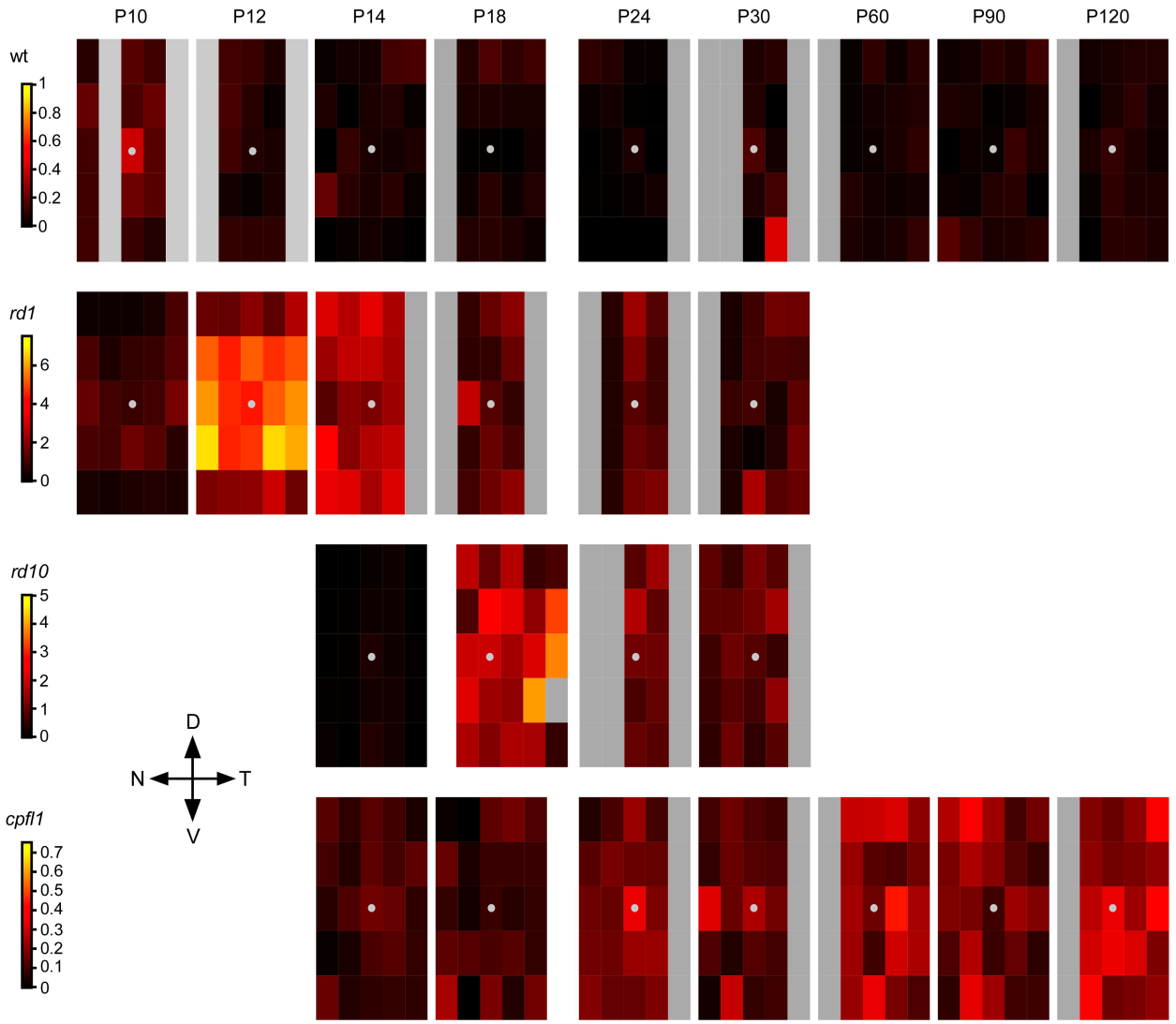
P10
P12
P14
P18
P24
P30
P60
P90
P120
wt
1
0.8
0.6
0.4
0.2
0
rd1
6
4
2
0
rd10
5
4
3
2
1
0
cpfl1
0.7
0.6
0.5
0.4
0.3
0.2
0.1
0
D
N
T
V

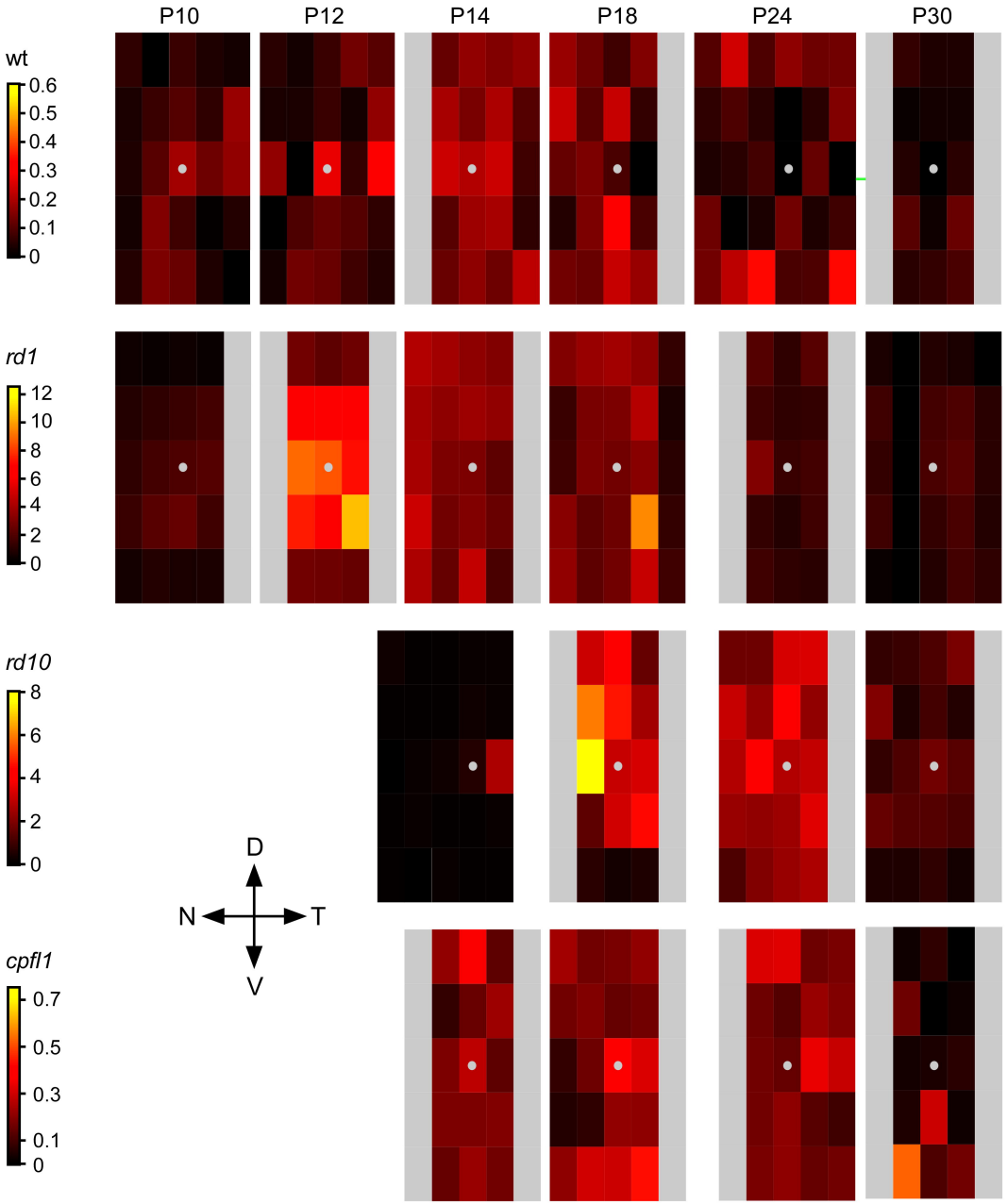
P10
P12
P14
P18
P24
P30
wt
0.6
0.5
0.4
0.3
0.2
0.1
0
rd1
12
10
8
6
4
2
0
rd10
8
6
4
2
0
cpfl1
0.7
0.5
0.3
0.1
0
D
N
T
V

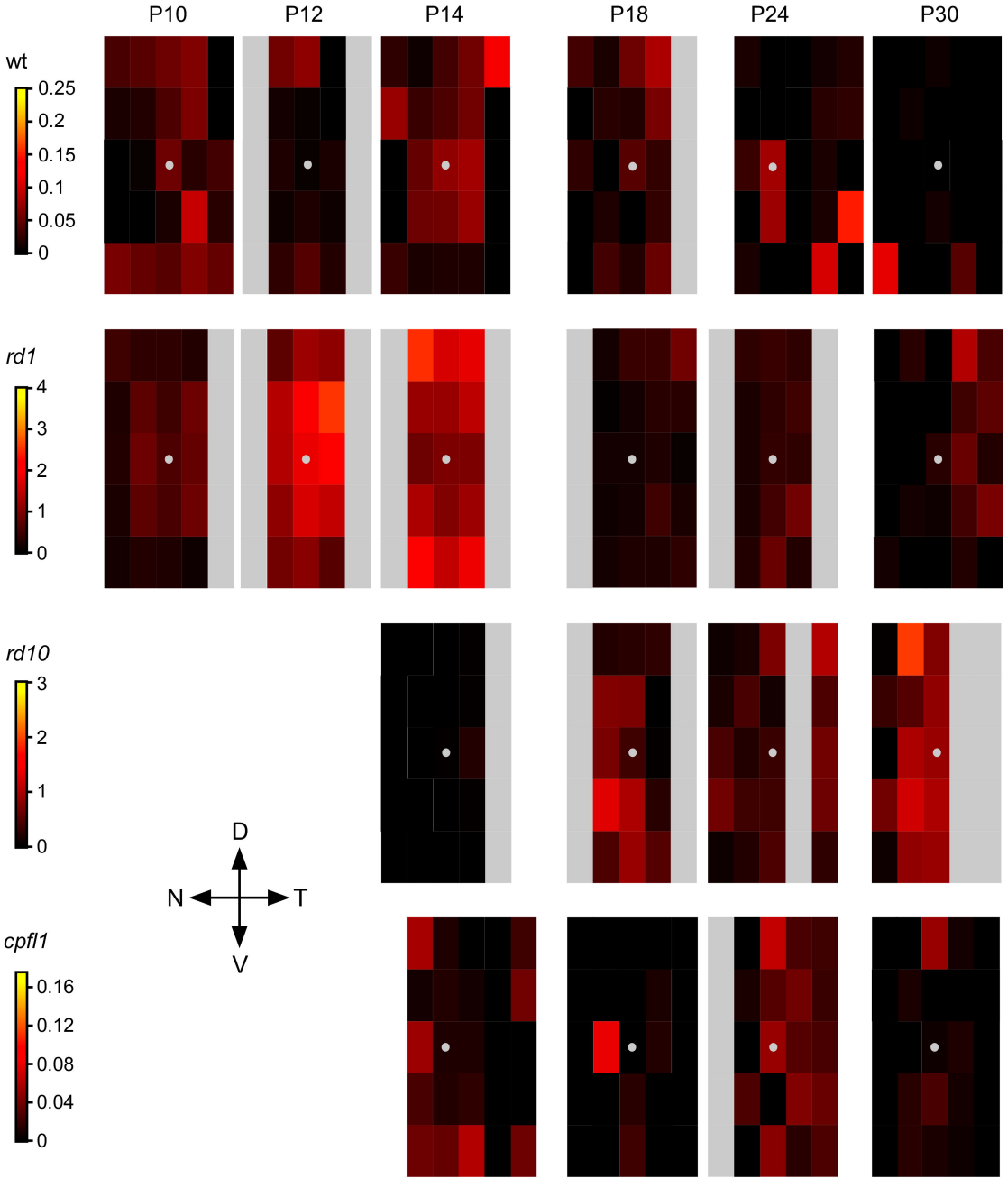
P10
P12
P14
P18
P24
P30
wt
0.25
0.2
0.15
0.1
0.05
0
rd1
4
3
2
1
0
rd10
3
2
1
0
cpfl1
0.16
0.12
0.08
0.04
0
D
N
T
V

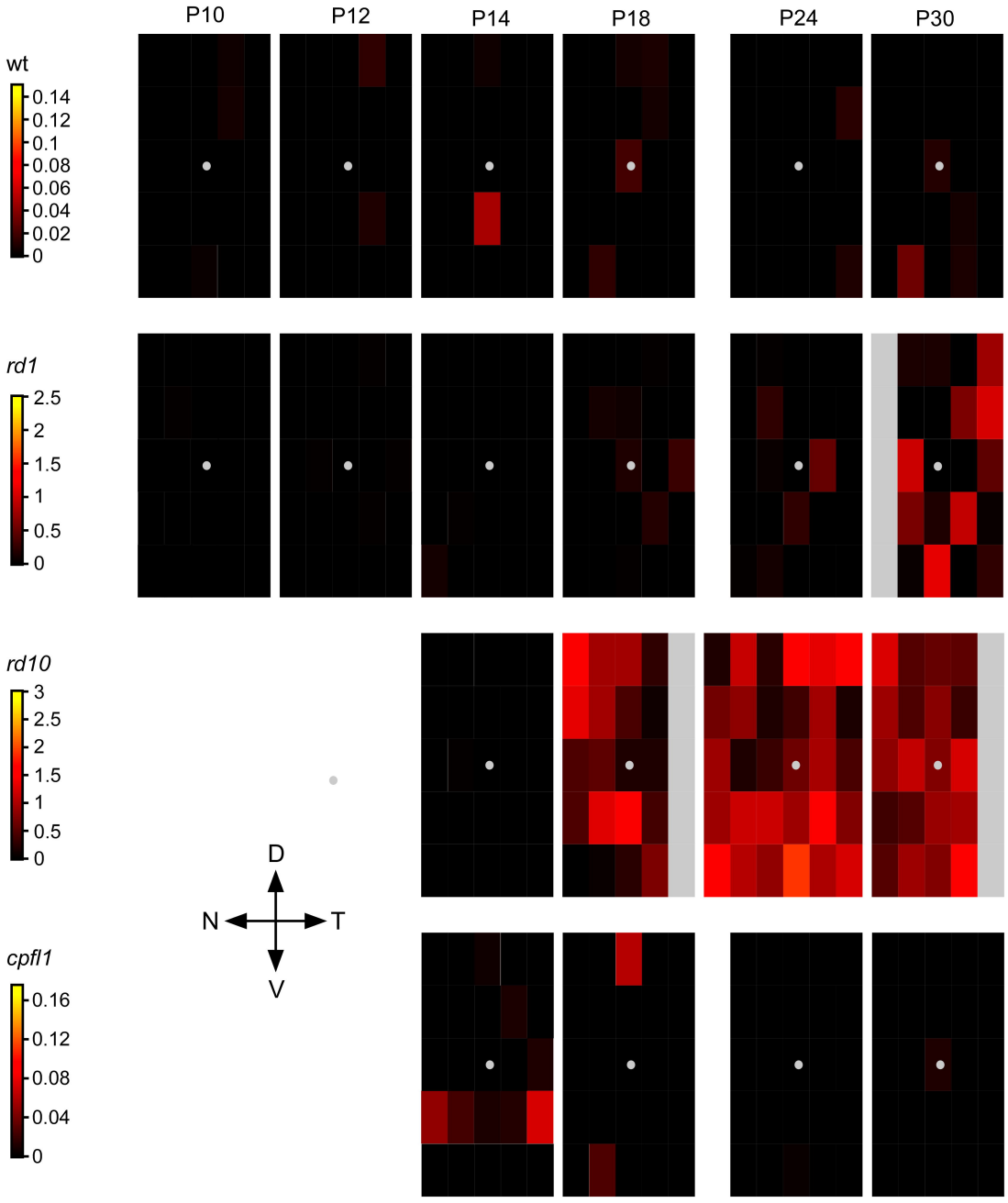
P10
P12
P14
P18
P24
P30
wt
0.14
0.12
0.1
0.08
0.06
0.04
0.02
0
rd1
2.5
2
1.5
1
0.5
0
rd10
3
2.5
2
1.5
1
0.5
0
cpfl1
0.16
0.12
0.08
0.04
0
D
N
T
V

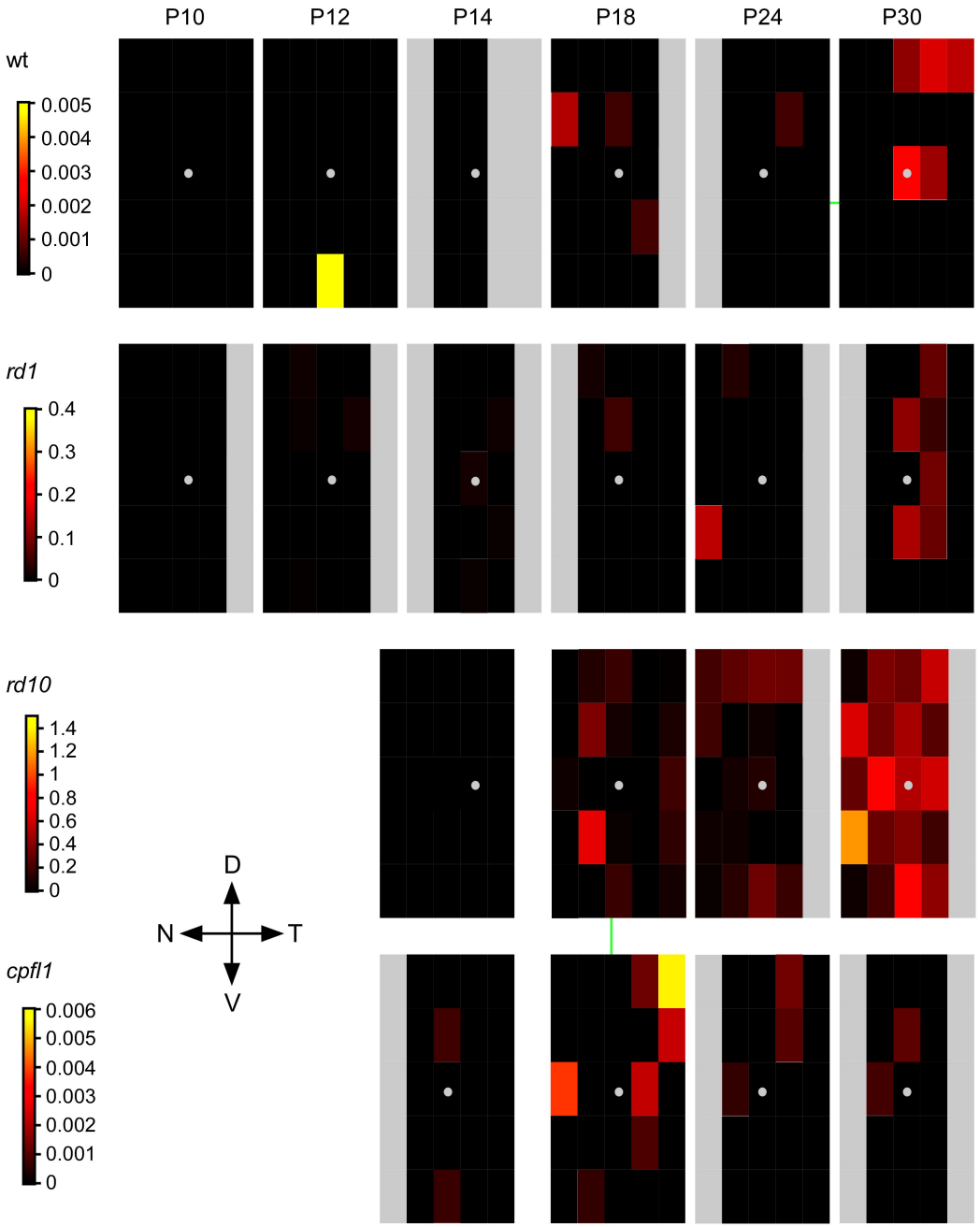
P10
P12
P14
P18
P24
P30
wt
0.005
0.004
0.003
0.002
0.001
0
rd1
0.4
0.3
0.2
0.1
0
rd10
1.4
1.2
1
0.8
0.6
0.4
0.2
0
cpfl1
0.006
0.005
0.004
0.003
0.002
0.001
0
D
N
T
V

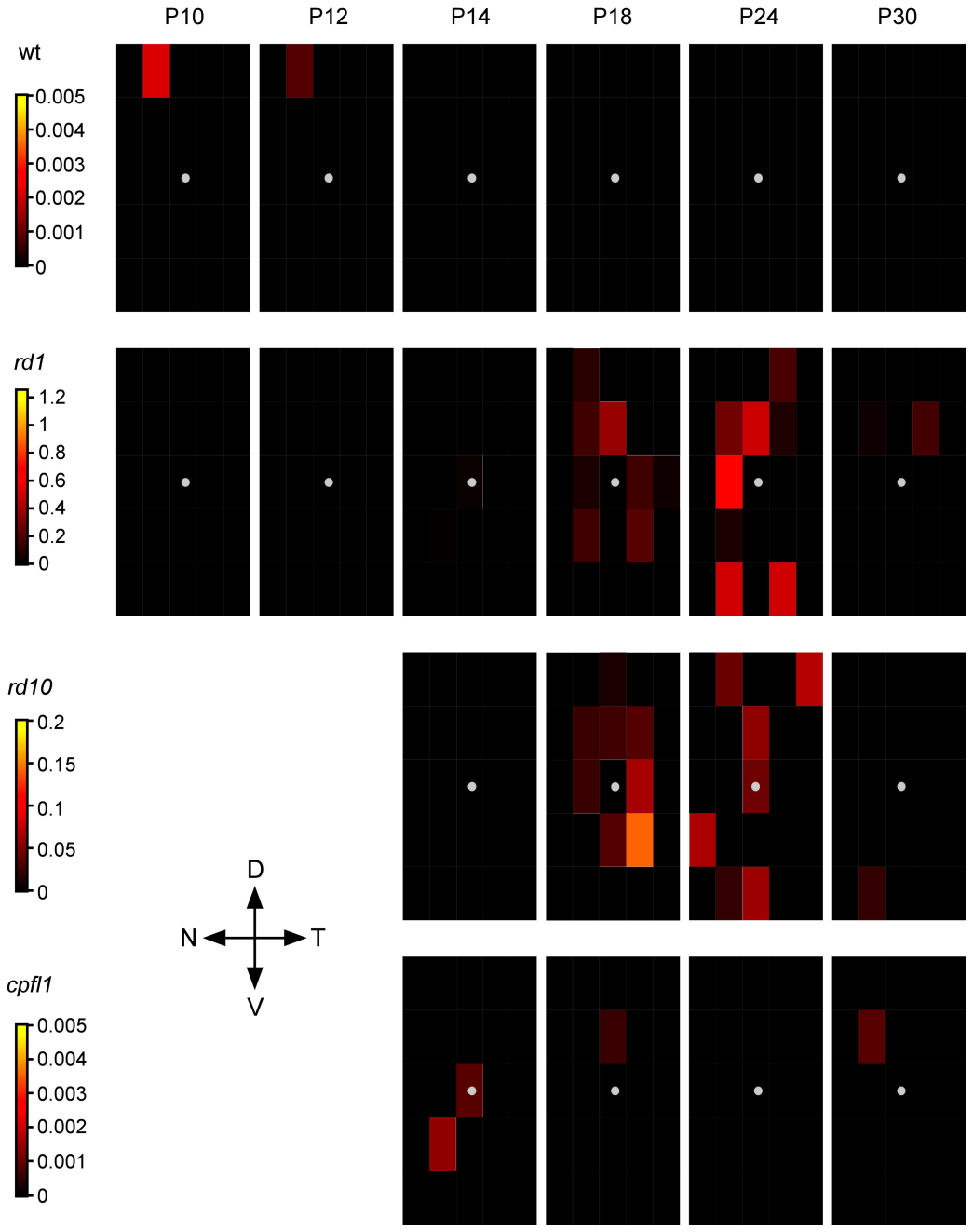
P10
P12
P14
P18
P24
P30
wt
0.005
0.004
0.003
0.002
0.001
0
rd1
1.2
1
0.8
0.6
0.4
0.2
0
rd10
0.2
0.15
0.1
0.05
0
D
N
T
V
cpfl1
0.005
0.004
0.003
0.002
0.001
0

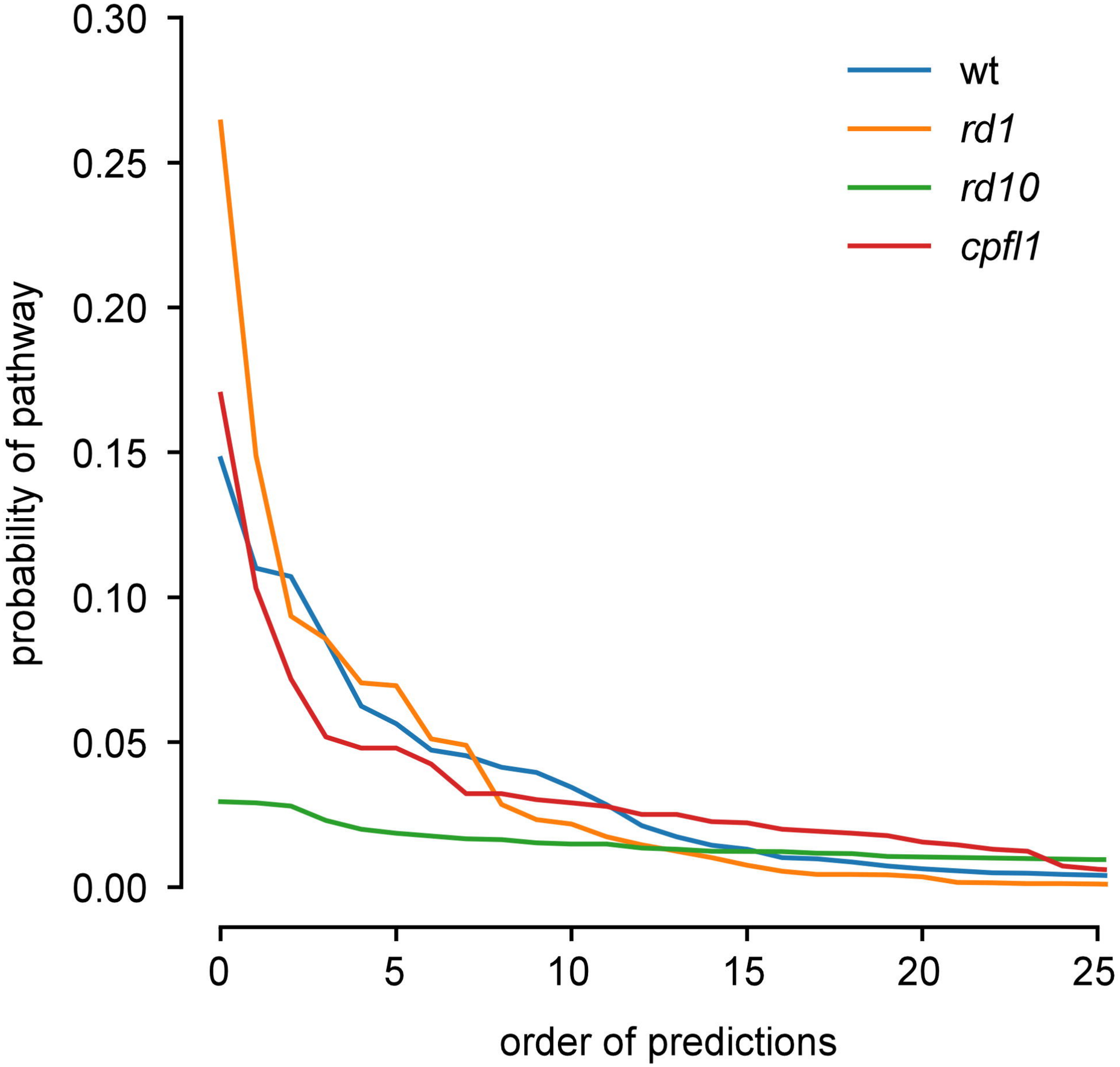
0.30
0.25
0.20
0.15
0.10
0.05
0.00
probability of pathway
0
5
10
15
20
25
order of predictions
wt
rd1
rd10
cpfl1